LASER ABLATION SAMPLING NEAR THE BREAKDOWN THRESHOLD

By

GRETCHEN E. POTTS

A DISSERTATION PRESENTED TO THE GRADUATE SCHOOL
OF THE UNIVERSITY OF FLORIDA IN PARTIAL FULFILLMENT
OF THE REQUIREMENTS FOR THE DEGREE OF
DOCTOR OF PHILOSOPHY

UNIVERSITY OF FLORIDA

2000

Copyright 2000

by

Gretchen E. Potts

To my family

ACKNOWLEDGMENTS

I would like to thank my research advisor Jim Winefordner for his confidence, support and guidance during my four years at the University of Florida. Jim has a passion for teaching not found in many professors. It was this passion that brought me to the JDW labs and which will guide me after graduation as I head to academia. I would also like to thank Ben Smith for his continuous patience and encouragement. As his teaching assistant in 2047 I learned a lot about spectroscopy as well as problem solving in research; he was able to calm my frustrations when I made mountains out of molehills. These two advisors have made our research group into a family and I can't imagine not being a member.

I would not have made it through this long journey without the support of friends. I would like to thank all Winefordner research group members, past and present, for their friendship and guidance. Those who contributed to my research include Dr. Igor Gornushkin, Dr. Bryan Castle, Dr. Ricardo Aucelio, Hossein Nasajpour, Shane Claggett, Irina Giurgiu and Qing Sun. I would specifically like to thank Dr. Nico Omenetto for his advice and understanding when my spirits were down. I could not have made it through graduate school without the emotional support of Joanne Bedlek Anslow, Dr. Andrea Croslyn, Dr. Wendy Clevenger Cory, Jason Keeton, Dr. Leslie King and Jason Wallace. I would also like to thank Dr. Giuseppe Petrucci for his guidance in the "big job search."

Jeanne Karably is known as the "glue" of the analytical chemistry division. I would like to thank her for enduring my endless questions. She also provided a kind ear in times of frustration.

My family has provided continuous support throughout my graduate career. Though they are one thousand miles away, we kept close through many phone calls and the internet. I am thankful for their wisdom and guidance. Their bi-annual visits afforded me a break from grueling research hours.

Finally, I would like to acknowledge the support of the staff and administration at the Particle Science Center, specifically Dr. Anne Donnelly, who always had an open door and heart. For financial support, I would like to acknowledge the National Science Foundation Engineering Research Center for Particle Science and Technology and their industrial partners.

Throughout my education, I have used music to express my feelings and emotions. Music is my outlet for daily struggles and frustrations that are encountered in research. It is fitting that I quote lyrics from Cole Porter's musical *Nymph Errant*. It is here that you find the answer to all questions... Experiment.

Be curious, though interfering friends may frown,
Get furious at each attempt to hold you down.
If this advice you'll only employ
The future can offer infinite joy
And merriment
Experiment and you'll see.

TABLE OF CONTENTS

page

ACKNOWLEDGMENTS iv

ABSTRACT viii

1 MATERIALS CHARACTERIZATION AND SURFACE TECHNIQUES FOR CHEMICAL ANALYSIS 1

- Introduction 1
- Surface Techniques for Chemical Analysis 2
- Intent of Work 4

2 ASPECTS OF LASER-MATERIAL INTERACTION 7

- Introduction 7
- Fundamentals of Laser Ablation and Plasma Formation 8
  - Gas breakdown 9
  - Solid breakdown 10
  - Features of a propagating plasma 12
- Atomic Emission within the Plasma 13
- Conclusion 15

3 THRESHOLD DETERMINATIONS 17

- Introduction 17
- Theoretical Threshold Determinations 17
- Experimental Threshold Determinations 19
- Influence of Laser Properties on Breakdown Thresholds 21
- Conclusion 22

4 INSTRUMENTATION AND EXPERIMENTAL CONDITIONS 24

- Experimental Set-up 24
- Sample Choice and Preparation 25
- Laser Properties 26
  - Laser power and pulse width 26
  - Laser irradiance and beam size 26

5 STUDY OF RESONANCE EMISSION OF Cu Ag Au AND Si 34

Introduction 34
Experiment 34
Results and Discussion 35
  Copper emission with a 532 nm laser 35
  Copper emission with a 1064 nm laser 36
  Silver emission with a 532 nm laser 36
  Silver emission with a 1064 nm laser 36
  Gold emission with a 532 nm laser 37
  Gold emission with a 1064 nm laser 37
  Silicon emission with a 532 nm laser 37
  Silicon emission with a 1064 nm laser 38
Conclusion 38

6 STUDY OF NON RESONANCE EMISSION OF Cu, Ag, Au AND Si 82

Introduction 82
Experiment 82
Results and Discussion 82
  Copper emission with a 532 nm laser 82
  Copper emission with a 1064 nm laser 83
  Silver emission with a 532 nm laser 83
  Silver emission with a 1064 nm laser 83
  Gold emission with a 532 nm laser 84
  Gold emission with a 1064 nm laser 84
  Silicon emission with a 532 nm laser 84
  Silicon emission with a 1064 nm laser 85
Conclusion 85

7 EFFECTS OF IRRADIANCE AND LASER WAVELENGTH ON THE ABLATION Cu, Ag, Au AND Si 128

Introduction 128
Experiment 128
Results and Discussion 129
  Determination of optimum delay and gate 129
  S/N versus laser irradiance 130
  Crater volume versus laser irradiance 131
  Signal versus crater volume 133
  Determination of breakdown thresholds 133
Conclusion 135

8 CONCLUSIONS AND FUTURE WORK 153

LIST OF REFERENCES 157

BIOGRAPHICAL SKETCH 162

Abstract of Dissertation Presented to the Graduate School
of the University of Florida in Partial Fulfillment of the
Requirements for the Degree of Doctor of Philosophy

LASER ABLATION SAMPLING NEAR THE BREAKDOWN THRESHOLD

By

Gretchen E. Potts

August 2000

Chairman: Dr. James D. Winefordner
Major Department: Chemistry

Laser-induced plasma spectroscopy (LIPS) is a new analytical method for materials characterization which uses the laser as the sampling and the excitation source. In LIPS, a short-pulsed laser is tightly focused onto a sample surface. During the pulse of the laser, the surface is heated beyond the latent heat of vaporization and material is ablated. The vaporized material develops into a hot plasma of high electron number density. The light emitted from the plasma is collected, dispersed and detected. Several laser and sample properties determine the threshold for ablation and subsequent plasma formation. The laser properties include laser irradiance, excitation wavelength, pulse duration and spot size. The sample properties include reflectivity, density, specific heat and latent heat of vaporization.

LIPS requires minimal or on sample preparation and can analyze any phase of matter. Requiring only optical access, LIPS has possible applications to online process monitoring. In the semiconductor industry, LIPS can provide spatially resolved

elemental identification. Depth-resolved analysis is also possible if the laser probes a sample repetitively in one location.

In this work, laser ablation and plasma formation are studied to further develop LIPS as a technique for spatially-resolved materials characterization. The laser is used to probe pure samples of copper, silver, gold and silicon. The first chapter of this dissertation provides an overview of materials characterization and presents LIPS as a useful alternative to the methods already in practice. Chapters two and three develop the theory behind the threshold for laser ablation and plasma formation and review previous research on the determination of ablation thresholds. Chapter four describes the instrumentation used. The time-resolved emission of the laser induced plasma is studied in chapters five and six. The emission is collected at 5 laser irradiances at two laser wavelengths: 532 nm and 1064 nm. The final experimental chapter (chapter seven) explores the effects of laser irradiance and wavelength on sample ablation volume. The ablation threshold is calculated for each sample studied.

CHAPTER 1
MATERIALS CHARACTERIZATION AND SURFACE TECHNIQUES FOR CHEMICAL ANALYSIS

Introduction

Materials characterization and design play an important role in technology. Scientists want to develop materials with ideal properties. Depending on the intended use of the material, several surfaces might be explored. For instance, corrosion and wear characteristics control a material's stability. This is especially evident in the automobile and medical prostheses industries. If the surface becomes damaged, the material loses function (1). In the electronics industry, surfaces are carefully fabricated through a systematic process so that the manufactured circuit performs its intended function (2).

The surfaces of most materials have specific requirements. Once the desired surface properties are determined and the surface is developed, how do scientists know whether they have achieved their goal? Emerging technologies require microanalytical techniques with well resolved spatial capabilities (3).

Surfaces are probed with 6 basic sources of energy: electrons, ions, neutrals, photons, heat or fields. The probed surface responds, emitting electrons, ions, neutrals, photons, heat or fields. In addition, these 6 sources are also the surface response. Therefore, 36 different classes of surface analysis exist (2). Each class has specific applications as well as surface requirements. A surface is characterized in three steps. Initially, a direct physical image of the surface is taken. Surface deformities as well as surface roughness are measured. This is followed by a structural analysis. Finally the surface composition is determined. These three steps usually require three separate methods of analysis. In addition, several techniques are used for elemental identification and composition (4). Table 1-1 summarizes the techniques most widely

Surface Techniques for Chemical Analysis

Auger electron microscopy (AES) is one of the oldest surface techniques. In 1923 Pierre Auger bombarded a gas with x-rays to cause β emission of electrons now known as Auger electrons. Electrons are the excitation probe as well as the surface response. Scientists now use primary electrons to probe the topmost atomic layers of samples to analyze Auger electrons. The electrons are only emitted within a small volume near the area in contact with the electron beam. This allows for high spatial resolution. AES is used primarily for conducting samples and is performed under high vacuum conditions (4). AES has a spatial resolution of 20 nm and a depth resolution of 1-20 nm. AES is commonly used for determination of metals, especially contamination segregation in metals (5, 6).

Similar to AES, x-ray photoelectron spectroscopy (XPS) detects electrons as the surface response. However, XPS uses x-ray photoelectrons as the excitation probe. Electrons for inner orbitals are ejected when bombarded by x-ray photons. The chemical composition is determined by measuring the electron binding energies (4). This technique is qualitative as well as quantitative. XPS has a spatial resolution of 8 μm and a depth resolution of 0.1 nm. XPS has been used to characterize several different surfaces from thin films (7) to proteins (8). These studies are performed on a dedicated XPS instrument. Recently, XPS has been explored as a on-line process monitoring tool in the semiconductor industry. The technique is useful in identifying defects monitoring the production of thin films (9, 10).

Secondary ionization mass spectrometry (SIMS) requires high keV primary ions. These ions bombard the surface ejecting secondary atomic ions and cluster ions. The ejected ions are detected with a mass spectrometer. Developed in the early 1960's, this technique was not employed for surface analysis until the 1980's. Although chemical information is obtained, SIMS is not ideal for quantitative analysis. It has a spatial resolution of 50 nm and the depth resolution is dependent on the measured intensity and the sputtering time (4). SIMS is useful in characterizing biochip surfaces (11), and is routinely used in the aluminum industry in production facilities as well as for surface finishing processes (12).

Low energy ionization spectroscopy (LEIS) and Rutherford back scattering (RBS) are two methods of ion scattering spectroscopy (ISS). In ISS, an ion beam is focused onto a surface. The ions collide with the surface atoms in a two-body collision. Backscattered ions from the primary beam are measured and their energy distribution is measured. The energy spectrum gives comprehensive information about the atomic masses on the surface (4). LEIS uses low energy ions (0.5-5 keV) and gives information on the top atomic layer. RBS uses high energy ions (several MeV) and gives depth information between 30 and 100 nm. RBS is an excellent method for the determination of thin films (13).

The laser is also used extensively in surface characterization. When coupled to an inductively coupled plasma mass spectrometer (ICP MS), the laser samples the surface and the plasma converts particles to atoms and finally ions for analysis by mass spectrometry. Several fundamental studies focus on LA-ICP MS (14-17). As a quantitative method, LA ICP MS is used to determine trace impurities in metals without matrix matched standards (18).

Laser-induced plasma spectroscopy (LIPS) is a new analytical method for surface characterization which uses the laser as both the sampling and the excitation source. LIPS requires minimal or no sample preparation and can analyze any phase of matter. Therefore, samples can be conductive or nonconductive, unlike AES, SIMS and XPS. Unlike LA ICP-MS, the sample is atomized and excited by one source, the laser plasma.

LIPS allows researchers to probe surfaces and gain knowledge of the local distribution of atoms rather than bulk averaging (19). The laser used in LIPS is commonly focused to a spot size of 50 – 100 µm for depth resolution as well as compositional mapping. Lasema and co-workers have published extensively on multielement chemical imaging and depth profiling of surfaces using LIPS (3, 19-27). Several of the papers focus on depth resolution and uniform crater formation. However, the size ablation crater as a function of laser conditions has not been thoroughly analyzed.

Intent of Work

The intent of this work is to explore laser-surface interactions as well as plasma formation to further the development of laser induced plasma spectroscopy (LIPS) as a surface analysis technique. Chapter two describes the background and theory behind laser-material interaction and plasma formation. Several studies on breakdown thresholds are reviewed in chapter three. Chapter four describes the experimental system. The following chapters detail experiments performed. The effects of laser irradiance on plasma emission and crater formation are analyzed. The studies also include the effect of excitation wavelength. Breakdown thresholds are determined theoretically and experimentally for several elements.

Table 1-1 Surface Techniques for Chemical Analysis (Adapted from O'Connor (2))

	Incident Probe		
Surface Response to Incident Probe	Electrons	Ions	Photons
Electrons	Auger Electron Spectroscopy (AES)		X ray Photoelectron Spectroscopy/ Electron Spectroscopy for Chemical Analysis (XPS/ESCA)
Ions		Low Energy Ionization Spectroscopy (LEIS) Rutherford Back Scattering (RBS) Secondary Ion Mass Spectrometry (SIMS)	
Photons			Laser induced Plasma Spectroscopy (LIPS)

CHAPTER 2
ASPECTS OF LASER MATERIAL INTERACTION

Introduction

In 1960, Maiman first observed emission of coherent radiation from the optical pumping of a ruby rod (28). The emission of coherent radiation was a direct result of a population inversion in an active medium, a ruby rod, resulting in amplification and oscillation. The word laser is derived from a phrase which describes the above process, light amplification by stimulated emission of radiation (29).

The laser provides coherent radiation with high average and peak power which allows for material ablation (30). Unlike conventional light sources, lasers have directionality and monochromaticity (31). Therefore, for the last forty years, lasers have become the mainstay of materials characterization and processing. Specifically researchers focused on the study of laser material interactions, the formation of laser plasmas, and the light emitted from the plasmas.

The first reported use of lasers for spectrochemical analysis was in 1962. Brech and Cross recorded a spectrum of elemental components in a microplasma following laser ablation (32). The plasma was formed using a normal pulsed ruby laser and a pair of electrodes.

Ablation studies in the 1960's were difficult due to the unreliability of lasers. Poor laser technology limited ablation studies primarily to theoretical investigations

Analytical studies were restricted to qualitative work, where the amount of laser energy was not critical (33).

The 1970's and 1980's brought lasers with shorter pulse lengths, higher peak power and more stability (30). Ruby lasers were replaced with neodymium doped lasers (Nd:Yttrium Aluminum Garnet and Nd:Glass). The solid state lasers had a more stable and optically superior beam, with one drawback. Most materials absorbed in the ultraviolet or visible region and Nd-doped lasers emit in the near infrared (33). Non linear optics solved this problem, providing frequency doubling, tripling and so forth (29).

Laser ablation was introduced commercially in the 1990's. Lasers are not only a part of everyday life, where they are used in a wide range of applications from compact disc players and medical surgery, but are also a vital part of industrial processing. Although laser ablation is commonly used commercially, the fundamentals of laser material interactions as well as plasma formation still require extensive research.

In laser-induced plasma spectroscopy, a short-pulsed laser is tightly focused onto a sample surface. The surface is heated beyond the latent heat of vaporization and material is ablated during the pulse of the laser. The vaporized material develops into a hot plasma of high electron number density. The light emitted from the plasma is collected, dispersed and detected. The following chapter discusses the processes involved in laser ablation, plasma formation and subsequent atomic emission.

Fundamentals of Laser Ablation and Plasma Formation

A laser induced plasma is generated by the breakdown of a sample to a totally ionized gas (34). Electron production and population growth, within the plasma, are dependent on the phase of sample at the focus of the laser. The theory for breakdown in gases forms the basis for breakdown in any phase.

Gas breakdown

Breakdown is initiated by ionization of the gas. The ionization can occur through two possible processes: impact ionization or multiphoton ionization (34). Impact ionization (Eq. 2-1) requires that initial electrons are in the focal volume and that the electrons have energy greater than the ionization energy of the sample gas. A neutral atom (M) is ionized by electrons that have sufficient energy to overcome the ionization energy.

(Eq. 2-1) $e^- + M \rightarrow 2e^- + M^+$

Electrons absorb laser radiation and convert the energy into kinetic motion. The electrons then collide with a neutral atom, ionizing the gas. Similar to a photomultiplier tube, one electron results in two electrons, which produce four electrons, etc. The electron concentration increases throughout the lifetime of the laser pulse which leads to a cascade breakdown (34).

During multiphoton ionization (Eq. 2-2), an atom (M) absorbs multiple photons. The additive energy of the photons increases until there is sufficient energy to promote an electron across the band gap of the element to the conduction band, forming an ion. The resulting electron can react with neutrals to form another metal ion and two electrons again resulting in the cascade breakdown (34).

(Eq. 2-2) $M + m\,h\nu \rightarrow M^+ + e^-$

In order to have breakdown in gases, a seed electron is necessary to have a cascade breakdown. The electron is either present in the focal volume or formed from the ionization of the sample gas. The probability for an electron to be present is quite low and therefore gases require high laser irradiances ($>10^8$ W/cm^2) for breakdown. Solids, however, can undergo breakdown at irradiances around 10^6 W/cm^2.

Solid breakdown

When focused on a solid, a pulsed laser beam can lead to several processes including heating, evaporation, degradation and several non-linear phenomena. For breakdown to occur, the processes of concern include the ejection of material from the surface and the formation of a plasma (35). Ablation and plasma formation occur in five steps: heating, melting, evaporation, atomization and excitation (36). It should be noted that it is not necessary to have a plasma in order for ablation to occur. Thresholds govern both ablation and plasma formation.

Laser material interactions begin with the heating of the sample surface by a laser beam. During the laser pulse, surface electrons absorb the incident photons of energy from the laser beam. The absorbed optical energy excites the electrons, increasing their kinetic energy. The energy causes the electrons within the sample to collide with each other. The kinetic energy from the collisions is converted to thermal energy, heating the lattice of the target material. Therefore, the optical energy from the laser pulse is converted into heat.

Thermal energy from electron collisions causes the temperature of the surface to rise by thousands of degrees. The temperature below the surface also rises due to heat conduction. If a sample has a high thermal conductivity, heat will dissipate quickly away from the sample surface.

The thermal energy on the surface continues to rise throughout the laser pulse and eventually surpasses the latent heat of vaporization. The temperature reaches a critical point. The incoming laser energy can no longer be dissipated from the focal point fast enough. The surface temperature rises, surpassing the boiling point and the result is evaporation (37).

Each sample has unique properties, which control the occurrence of evaporation; these properties are thermal diffusivity, density and the latent heat of vaporization. For a constant laser pulse duration, the estimated minimal laser irradiance for evaporation to occur can be calculated.

After time t (s), the thickness of the heated material is dependent on the density (ρ (g/cm³)) the thermal conductivity (λ (J/ s cm K)) and the specific heat (C_p (J/g K)). The evaporation will only take place if the energy density exceeds the latent heat of vaporization of the material (L_v, (J/g)). The time for this all to occur (t_v (s)) should be less than the pulse duration (t_p (s)). The above conditions are expressed in equation 2-3 (38). The minimum irradiance for ablation is termed E_{min}.

(Eq. 2-3)
$$E_{min} = \left(\frac{\rho\lambda}{t_v C_p}\right)^{1/2} L_v$$

Sample conditions also govern the time (t_v (s)) to reach the boiling point of the material (Eq. 2-4). T_v (K) is the vaporization temperature and T_o (K) is the initial surface temperature (39).

(Eq. 2-4)
$$t_v = \frac{\pi\lambda\rho C_p (T_v - T_o)^2}{4E^2}$$

The temperature of the surface (T_s (K)) and the rate of material removal (v_m (g/s)) are represented in equations 2-5 and 2-6 (37).

(Eq. 2-5)
$$T_s = \frac{2E}{\lambda}\left(\frac{\lambda t_v}{C_p \pi}\right)^{1/2}$$

(Eq. 2-6)
$$v_m = \frac{E}{\rho\left[L_v + C_p (T_v - T_o)\right]}$$

Following laser ablation, the vapor phase formed above the sample surface is partially ionized. Similar to the mechanism for breakdown in gases, which require a seed electron, significant ionization is needed for breakdown in solids. Thermally generated electrons in the vapor phase absorb incoming laser radiation through inverse Bremsstrahlung absorption forming a plasma. The absorption causes heating which results in subsequent expansion of the plasma (36). Bremsstrahlung is derived from the German words meaning to "slow down radiation" (34). An inverse Bremsstrahlung process describes electrons gaining energy in a laser field.

For plasma production, two important assumptions are made. It is assumed that the laser beam is spatially and temporally uniform within the pulse duration, and the molten material ejected is negligible compared to that of atomic ejection (i.e. the plasma) (26).

Features of a propagating plasma

As a plasma absorbs laser energy, it decreases the amount of energy reaching the target. The absorption is a result of inverse Bremsstrahlung collisions and is proportional to the square of the laser wavelength (40). The mechanism is referred to as plasma shielding. The plasma is shielding the surface from further laser interactions.

Under ideal conditions, a plasma will expand throughout the duration of the laser pulse. However, as the plasma expands, the laser also heats the atmosphere. The atmospheric heating occurs along the same axis as plasma formation. A graphic depiction of this can be seen in Figure 2-1. The region of atmosphere, which is heated, absorbs laser radiation. The absorbing region attenuates the laser radiation which reaches the plasma.

Atomic Emission within the Plasma

Following laser ablation and plasma formation, temperatures within the plasma can reach 25000 K (34). The electron number density can be as high as 10^{19} cm^{-3}. In emission spectroscopy, these conditions describe an ideal excitation source. The energy is sufficient to atomize the analyte and to excite the element or elements of interest (29).

In the excitation process, electrons from lower energy orbitals are promoted to higher orbitals. If an electron is initially in the ground state, the electron transition is referred to as a resonance transition. Following excitation, the excited atoms quickly relax to the ground state, emitting electromagnetic radiation (41). The frequency of the radiation is characteristic of the electronic transition. The Boltzmann distribution relates the number of atoms n_i (cm^{-3}) in an energy level i to the total number of atoms n_0(cm^{-3}), where g_i is the statistical weight of level i, E_i is the excitation energy (J) relative to the ground state, k is Boltzmann's constant (1.38 x 10^{-23} J/K), T (K) is the absolute temperature and Z(T) is the partition function over all states. (Eq. 2-7) (29)

(Eq. 2-7)
$$n_i = \frac{n_0 g_i e^{-\frac{E_i}{kT}}}{Z(T)}$$

(Eq. 2-8)
$$\Phi_E = A_{ji} h \nu_{ji} n_j V$$

Equation 2-8 expresses the radiant power of emission Φ_E as a function of population density in the excited state n_j (cm^{-3}), the Einstein transition probability A_{ji} (s^{-1}), the frequency of the transition ν_{ji} (s^{-1}) and Planck's constant, h (6.626 x 10^{-34} Js). From equations 2-7 and 2-8, it can be inferred that the radiant power is proportional to the excited state population density and as a result to the analyte concentration (29).

The emitted radiation is a combination of radiation from each electronic transition. A monochromator is used to spatially disperse the radiation into spectral lines. In general, individual spectral emission lines are a symmetric distribution of wavelengths about a mean which is the maximum intensity for the emitted radiation (41). The mean wavelength corresponds to the energy difference between the energy levels. In a laser-induced plasma, broadening of the emission line is due to Doppler and pressure broadening (42).

In Doppler broadening, a shift is observed in the electromagnetic radiation. The shift is a result of the atom (which is emitting the radiation) moving away from the detector. In the plasma, atoms are moving in every direction with a Maxwell-Boltzmann velocity distribution (41). The atoms which move perpendicular to the detector, along the axis of detection, cause the spectral line to be broadened.

Pressure broadening is caused by collisions between emitting species and other atoms, ions or electrons. In a plasma, three types of collisons are important: resonance interaction, Stark broadening and Van de Waals interactions. If the collison occurs between two identical atoms, the broadening is called a resonance interaction. When an emitting atom is perturbed by the electric field of an ion or electron, the result is Stark broadening. Van de Waals broadening occurs when two neutral particles interact (42).

Temperature inhomogeneity is another process which affects the spectral line profile. A cooler region of the plasma, containing unexcited atoms, surrounds excited atoms in the center of the plasma. Radiation emitted as a result of resonance transitions can be absorbed by the atoms in the cooler region (41). The self-absorption results in a dip in the center of the resonance emission line. The dip in the spectral line caused by the temperature gradients within the plasma is called self-reversal.

Conclusion

The theory above describes the events involved in laser ablation, plasma formation and atomic emission. Laser-induced plasma spectroscopy is an analytical tool which involves all three of these phenomena. Several parameters (described in this chapter) affect laser ablation, plasma formation and propagation. Additional parameters (also described) influence atomic emission. The effects of these parameters on the ablation of copper, silver, gold and silicon will be explored in further chapters.

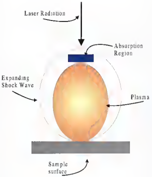

Figure 2-1 Schematic of a propagating plasma (34)

CHAPTER 3
THRESHOLD DETERMINATIONS

Introduction

The breakdown threshold is defined as the critical level at which a laser ablates a sample and the vaporized sample develops into a plasma. Several theoretical expressions have been derived to calculate the breakdown threshold (38, 43, 44). Researchers have also determined the breakdown threshold experimentally (45-54). Theoretically, researchers consider sample properties in breakdown calculations. Important properties include reflectivity, thermal conductivity, heat capacity and density. Experimentally, researchers have varied laser wavelength, pulse duration and beam size.

Theoretical Threshold Determinations

Many references discuss the theory behind calculated thresholds. An early mention of threshold calculations is found in the *Laser Handbook*, written in 1972 (43). Krokhin proposes a condition for estimating the minimal laser power density. The condition is shown in equation 3-1 where U is the sublimation energy (erg g^{-1}), a is the coefficient of thermal diffusivity ($cm^2\ s^{-1}$) and τ is the duration of the laser pulse (s).

(Eq. 3-1) $$q_0 > q_e = \rho U\left(\frac{a}{\tau}\right)^{\frac{1}{2}}$$

In the equation q_0 (erg $cm^{-2}\ s^{-1}$) is the laser power density and q_e (erg $cm^{-2}\ s^{-1}$) is the minimal laser power density needed for evaporation. For ablation to occur, the laser power density should exceed the minimal laser power density. Krokhin also states that high-energy laser radiation ($q_0>q_c$) causes evaporation, atomic excitation and ionization, the condition needed for optical breakdown.

Moenke-Blankenburg uses Krokhin's ideas as a basis for a threshold equation in *Laser Ionization Mass Analysis* (38). An introductory background on lasers and laser target interaction is given. The threshold equation is described as the minimum absorbed power density E_{min} (W/cm^2), below which no evaporation will occur (see Equation 2-3). Using a high power density laser, a sample will be evaporated and develop into a laser plasma.

Arnold and co-workers present a method for determination of the threshold fluence (44) using computer simulations. The non-stationary averaging is used to study a surface thermal evaporation model. The averaging allows for study of the influence of temperature on specific heat, thermal conductivity and absorptivity and the influence of the laser temporal profile. The authors modeled the theoretical ablation depth as a function time over the duration of a laser pulse. They found that the ablation curve has three regions which describe how the laser energy interacts with the material over time. The region characterized by material heating is referred to as the Arrhenius region. The Arrhenius region occurs at laser fluences below the breakdown threshold. A linear equation describes the region where the crater depth is linear with laser fluence. The third region (the screening region) is characterized by plasma shielding and is observed at fluences above the threshold.

From the equations describing the linear region, the authors derived an equation to calculate the theoretical breakdown threshold fluence.

(Eq. 3-2) $$\phi_{th}=\frac{H_v(l+\alpha^{-1})}{A}$$

In equation 3.2 the threshold laser fluence (ϕ_{th}) is directly proportional to the volumetric enthalpy at the surface (H_s) and indirectly proportional to the sample absorptivity (A). The thermal length is expressed as *l* and the absorption length is expressed as α.

Experimental Threshold Determinations

Although calculations are helpful in predicting ablation thresholds, it is important to recognize that all factors necessary for plasma formation might not be considered. Therefore, it is useful to compare theoretical calculations with experimental determinations. Although some researchers use microscopy to study the ablation thresholds, most probe the plasma during formation to determine thresholds for ablation.

Stuart and co-workers used light microscopy as well as scanning electron microscopy to investigate the breakdown threshold of gold coatings (45, 46). A Ti:Sapphire laser was pulsed between 0.1 and 1000 ps to evaluate the dependence of laser-ablation on pulse-width. For laser pulses >30 fs, the authors suggest the breakdown is a two-fold process: multiphoton ionization followed by cascade ionization. The breakdown is initiated with the formation of electrons from multiphoton ionization. Upon further heating by the laser, the electrons collide leading to a cascade breakdown. The result is an exponential increase in electron concentration with time. For ultra-short pulses (<30 fs), multiphoton ionization was responsible for the damage.

Some researchers have used an additional laser pulse to determine thresholds by reflective optical probing (47, 48). Femtosecond laser pulses were focused onto the sample surface to form a plasma. A pump-laser was used to monitor the plasma during formation. The authors assume that the threshold is surpassed when a sharp increase in the optical reflectivity of the sample surface is detected. As the plasma developed, the electron number density reached a critical value. The increase in electron number density resulted in a change in the optical reflectivity of the plasma. The authors defined the threshold breakdown as the laser fluence at which the optical reflectivity sharply increases. As the plasma developed, the optical reflectivity was also measured. Thresholds were found for glass (2.8 x10^{13} W/cm^2), MgF_2 (1.5 x10^{13} W/cm^2), sapphire (1.3 x10^{13} W/cm^2) and fused silica (1.0 x10^{13} W/cm^2).

Other researchers have extrapolated the breakdown threshold from the ablation volume (49). Using a Ti sapphire laser, optical breakdown was studied for pulse duration between 5 ps and 5 fs. Plots were made of ablation volume (V_a) versus laser fluence (J/cm^2). A linear relationship was found and a regression line was fit to the data. The threshold was determined by solving the regression equation for $V_a = 0$. Typical thresholds ranged between 2-4 J/cm^2.

Similarly, researchers have used extrapolation to determine the threshold fluence based on plots of signal-to-noise (S/N) versus laser fluence (50). The authors propose that the breakdown threshold is the minimum fluence needed to detect an emission signal. They define the limit of detection as a S/N ratio of 3 for the most intense emission line. Therefore, the breakdown threshold is the laser fluence at which a S/N ratio of 3 is obtained. A Q-switch Nd:YAG laser (266 nm, 532 nm and 1064 nm) generated the laser induced plasma. Light from the plasma was dispersed and detected with an intensified charge coupled device (ICCD). Excitation wavelengths as well as fluence were varied for each metal studied. The breakdown thresholds were calculated using Moenke-Blankenburg's expression (38). A comparison of the calculated thresholds and the experimental thresholds for Cu and Ag are given in Table 3.1. The calculated thresholds are 2 times the experimental values.

A recent technique for threshold determination evaluated pressure waves generated during plasma formation (51). A He Ne probe beam is passed parallel to the target. A deflection of He Ne beam indicates the presence of a pressure wave. The angle of deflection allowed an absolute measurement of the pressure amplitude. The authors determined the threshold fluence for Ti, Ni, Mo, Cu, W, Au and Al. Of particular interest are the breakdown thresholds for Cu (0.45 GW/cm^2) and Au (0.99 GW/cm^2).

Influence of Laser Properties on Breakdown Thresholds

The laser fluence and spot size were varied by Marcus and co-workers (52). Previous papers have shown that the energy of the laser is deflected outside the focal area by the expanding plasma when the laser beam size is around 0.03 cm^2 (55). At larger beam sizes, more energy remained within the focus, enhancing the expanding plasma. The spot size of a 500 J CO_2 laser was varied using a focusing mirror along the optical axis. The authors calculated the thermal coupling coefficient as the ratio of the thermal energy absorbed to the laser pulse energy. Enhanced thermal coupling was observed for larger spot sizes.

The dependence of breakdown thresholds on pulse duration was studied theoretically by Niemz (53). The proposed model gave a consistent theory to explain the square root dependence of breakdown thresholds on pulse durations in the picosecond and nanosecond time regimes. Plasma properties considered included avalanche ionization, electron-ion recombination and electron diffusion. The theory supported previous experimental work on thresholds which found the square root dependence but had no comprehensive explanations.

Using an acoustic method for determining breakdown thresholds, Apostol and co-workers studied the effects of spot area and target density on ablation (54). YBCO superconducting targets were studied with an UV laser (266 nm). The YBCO samples were prepared in two different densities, 86% and 92%. The threshold fluences were determined at both densities for various laser spot sizes. Table 3-2 summarizes the findings. The threshold fluence at the 92% YBCO density is roughly twice the fluence at the 86% YBCO density. For both sample densities, the threshold fluence decreases with increasing laser spot size.

Conclusion

The above review discusses the experimental and theoretical determination of breakdown thresholds. Choice of an experimental method for breakdown determination may also depend on available instrumentation. The methods, which involve extrapolation of plots of ablation volume and S/N, are most useful as they do not require additional lasers for probing the plasma.

Table 3-1. Breakdown thresholds determined experimentally for various metals (50)

Element	Theoretical Threshold (GW/cm^2)	Experimental Threshold at specified wavelength (GW/cm^2)		
		266 nm	532 nm	1064 nm
Cu	0.656	1.29	0.322	0.292
Ag	0.460	1.08	0.316	0.234

Table 3-2. Threshold fluences found for two YBCO sample densities at various spot sizes (54).

Spot Area (cm^2)	Threshold Fluence at 86% Sample Density (J/cm^2)	Threshold Fluence at 92 % Sample Density (J/cm^2)
1.32	0.18	0.34
1.83	0.09	0.19
3.58	0.08	-
4.34	0.07	

CHAPTER 4
INSTRUMENTATION AND EXPERIMENTAL CONDITIONS

Introduction

For materials analysis, an existing laboratory instrument was tailored to fit the research needs. In addition, several parameters and procedures were established which would remain consistent throughout the experiment. It was important to determine the pulse width of laser as well as the average laser energy for each experiment. A computer program was written to facilitate data work up.

Experimental Set up

A schematic of the laser ablation instrument is shown in Figure 4-1. The instrument has three major components. A laser and accompanying accessories provide the excitation energy. The laser is then focused through a laboratory built microscope for ablation. Finally, the emitted radiation is collected with optics, dispersed and detected. The components are explained below. The instrument was controlled with a Pentium computer. Table 4-1 lists all components and respective manufacturers.

The Nd:YAG laser operates at 1064 nm. Figure 4-2 is a schematic of the laser. The laser cavity was modified with a doubling crystal, a dichroic mirror and filter assembly. The 1064 nm radiation passes into the crystal. The radiation that is frequency doubled to 532 nm. Both 532 and 1064 excitation leave the crystal and interact with a dichroic mirror. The mirror is positioned at 45° to the incident beam. It is coated to reflect 1064 nm and pass 532 nm This mirror can be removed when 1064 nm radiation is desired

The laser beam (either 1064 nm or 532 nm) enters the microscope perpendicular to the axis of excitation (see Fig. 4-3). In order to bend the light, a second dichroic is used to direct the laser light through the microscope This mirror is specifically coated to only reflect radiation around 532 nm and 1064 nm and passes all other radiation Therefore, visible radiation passes through the mirror which is necessary for viewing the sample by the CC TV camera

A three lens focusing system inside the microscope focuses the light into the objective The focal distance of these lenses is given in Figure 4-3 The objective is 10x The sample was placed on a xyz translation stage for each experiment. The z-translation was used to focus the microscope

Following ablation a two-lens scheme was used to collect the plasma emission and focus it into the spectrometer The first lens collected the emitted light from the plasma The second lens focused the emitted light into the spectrometer The spectrometer had three gratings 1200 2400 and 3600 grooves/mm Gratings were chosen for each experiment and were dependent on the desired conditions. The light was dispersed with one of the three gratings and detected with an Intensified Charged Coupled Device (ICCD) The ICCD had a pulse generator and controller which allows for gating

Sample Choice and Preparation

Copper silver gold and silicon were chosen for study Copper and silver plates were purchased from Alfa Aesar (Ward Hill MA) The plates were 3 125 mm thick and are 99.95% pure (metals basis). The silicon wafer was obtained from Dr. David Johnson (Plasma-Therm, St. Petersburg, FL). The wafer is of ultra-high purity. The gold sample was a coin purchased from National Coin (Gainesville, FL). It had 99.5% purity. Prior to analysis, each surface was cleaned with ethanol to remove any surface contaminants. The samples were dried using nitrogen gas.

Laser Properties

Laser power and pulse width

A calorimeter measured the average laser power at the output of the focusing optics. A transducer dial on the front of the power supply controlled the laser power. However, the pulse width varied with the dial position. Figure 4-4 shows how the pulse width varies with dial setting. Therefore, a constant position was needed for all experiments. Glass band pass filters were used to attenuate the laser power. The filters were combined into sets for attenuation. These sets are described in Table 4-2.

Laser irradiance and beam size

As explained above, the average laser power was measured with a calorimeter. In order to calculate irradiance, E (W/cm^2), from this average power, P_{avg} (W), equation 4-1 is used.

(Eq. 4-1)
$$E = \frac{P_{avg}}{\tau f A}$$

In this equation, τ is the pulse width of the laser (12.2 ns). The frequency of the laser is f (10 s^{-1}). The area of the laser beam, A (cm^2), is $2\pi r^2$ where r (cm) is the radius of the beam. The radius of the beam was measured using three techniques: the size of laser burn on photographic paper, the size of a hole formed following the ablation of a gold leaf and size by response to a razor edge.

In the first technique, photographic paper was placed at the focus of the laser. A single shot was fired from the laser. Next, the size of the burn on the paper was measured. The burn technique yielded a spot size of 500 µm. The spot size was obviously too large for light that was focused through a microscope. The photographic paper was very sensitive to light. Consequently, the burn spot on the paper was much larger than the actual beam size.

The second technique used to measure the spot size involved gold leaf. Gold leave was affixed to a glass slide with double stick tape. The slide was then placed at the focus of the laser and a single shot was fired. The size of the hole in the gold foil was measured with optical microscopy. The spot size of 170 µm was also too large. As explained in chapters 2 and 3, several processes determine the ablation of a sample. Though the gold foil was a thin layer, the ablation was dependent on several properties of gold, and therefore not an accurate technique for measuring the spot size.

The most accurate technique used to measure the laser spot size was the razor. The edge of the razor was passed through the focus of the laser beam using a micrometer screw. The intensity of the laser was measured with a fast photodiode with respect to the position of the razor edge (Figure 4-5A). The first derivative plot of the intensity versus the edge position gave an accurate determination of spot size (Figure 4-5B). A Gaussian curve was fitted to the first derivative plot. The full width half maximum (FWHM) of the Gaussian fit determined the spot size to be 19 µm.

Table 4-1. Instrument components and manufacturers

Specific Component	Company	Location
YQL-102 Nd:YAG Laser	Laser Photonics	Orlando, Florida
NEC CC TV Camera	Fisher Scientific	Atlanta, GA
Toshiba Television Monitor	Fisher Scientific	Atlanta, GA
Unislide Translation Stage and Controllers	Velmex, INC	Bloomfield, NY
Calorimeter (#360101)	Scientech	Boulder, CO
Spectra Pro 500 0.5 m Spectrometer	Acton Research	Trenton, NJ
ICCD 576S (576x384)	Princeton Instruments	Trenton, NJ
PG 200 Pulse Generator	Princeton Instruments	Trenton, NJ
Detector Controller	Princeton Instruments	Trenton, NJ
200 MHz Personal Computer	CyberMax Computer, INC	Allentown, PA
Various Dichroic Mirrors	Laser Optics	Danbury, CT
10X Microscope Objective	Zeiss	West Germany

Table 4-2. Filter sets used for laser power attenuation

Laser Wavelength (nm)	Filter Set	Fraction Transmitted	# of Filters Used
532	A	0.09	4
	B	0.18	3
	C	0.26	3
	D	0.50	1
	E	0.81	1
1064	A	0.0005	2
	B	0.009	3
	C	0.016	4
	D	0.026	3
	E	0.044	4

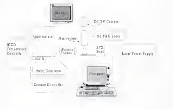

Figure 4-1 Schematic diagram of LIPS set up.

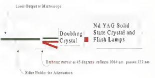
Laser Output to Microscope
Doubling Crystal
Nd YAG Solid State Crystal and Flash Lamps
Dichroic mirror at 45 degrees reflects 1064 nm passes 532 nm
Filter Holder for Attenuation

Figure 4-2 Schematic diagram of laser cavity

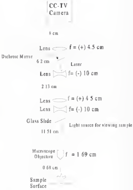

Figure 4-3 Microscope geometry

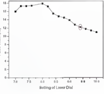

Figure 4-4 Plot of pulse width versus setting of high voltage control. For each experiment, the laser dial is set at 9.4, corresponding to a pulse width of 12.2 ns

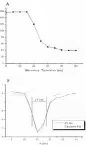

Figure 4-5 Determination of laser spot size. (A) Photodiode response versus razor edge position. (B) First derivative plot of (A)

CHAPTER 5
STUDY OF RESONANCE EMISSION OF Cu Ag, Au AND Si

Introduction

Though several researchers have developed theories on laser ablation mechanisms (34 37 38 44 45) It is still quite difficult to gain a complete view of the ablation process without experimentation Therefore, an understanding of signal diagnostics is essential to understanding the energetic ablation process (56) Researchers have used light microscopy pressure waves and optical refractivity to monitor the plasma (45 47 51) A simple technique for the monitoring of laser ablation is time resolved spectroscopy Light from the plasma is collected at several delays throughout the lifetime of the plasma. The emission spectra reveal information about the expanding plasma. In the next two chapters the time-resolved spectra of copper silver gold and silicon will be examined. The four elements are common components in the semiconductor industry In this chapter we will discuss the evolution of resonance lines generated in a plasma formed from the ablation of a sample with a Nd YAG laser operated at both 532 and 1064 nm

Experiment

The experimental set up is described in Chapter 4 Each sample was ablated using 532 nm and 1064 nm laser radiation at five different fluxes Day to-day fluctuations in the power supply were accounted for by measuring the laser power with a calorimeter at the start of each experiment The laser was attenuated so that the 5 irradiances used were generally the same for each experiment. Table 5.1 lists the measured power for each data set taken as well as the calculated incident irradiance. The irradiances had 5% uncertainty. Laser irradiance is expressed as power per unit area incident on the sample. One can see that the irradiances are very similar for each experiment. For simplicity purposes, the irradiances from the resonance emission of copper with 532 nm excitation will be used for all discussions. The irradiances were 2.3 GW/cm^2, 4.7 GW/cm^2, 6.8 GW/cm^2, 11 GW/cm^2 and 21 GW/cm^2.

Time resolved emission from each sample was collected at the several gate delays with a gate width of 0.3 µs. The delay intervals were -0.1 µs, 0.2, 0.6 µs, 1.0 µs, 1.6 µs, 2.4 µs, 3.4 µs. At the earliest delay, emission was collected for -0.1 µs before ignition of the plasma. The emission was collected for 0.3 µs- 0.2 µs past time zero. Table 5-2 lists the resonance line studied for each sample.

Results and Discussion

Copper emission with a 532 nm laser

Figures 5.1, 5.2, 5.3, 5-4 and 5-5 show the time-resolved emission spectra for copper at five increasing laser irradiances with a 532 nm laser. The prominent resonance lines observed for copper were 324.754 and 327.396 nm. As the resonance lines evolve self reversal is a prominent feature. It is visible at every laser fluence and delay time at which the resonance lines are visible. The self-reversal feature indicates that there is a significant temperature gradient in the plasma.

At the lowest irradiance (Fig. 5.1), the resonance emission lines evolve quickly. Emission is observed at the shortest delay times at the lowest irradiance. The resonance line disappears from the spectrum by 0.6 µs after the plasma ignition. As the laser irradiance increases, the plasma emission is sustained longer At an irradiance of 4 7 GW/cm^2 (Figure 5 2) the plasma emission disappears at 1.0 µs The three highest irradiances sustain plasma emission for as long as 1 6 µs (Figs 5-3 5-4 and 5-5)

Copper emission with a 1064 nm laser

For comparison the same copper target was sampled with the laser at 1064 nm Figures 5-6, 5 7, 5-8 5-9 and 5 10 show the time-resolved emission spectra for copper at the five laser irradiances Once again self reversal is a prime feature. The emission at the lowest irradiance (Fig 5-6) persists until 1 6 µs, which is longer than at 532 nm. The emission with 1064 nm laser radiation is sustained longer that with 532 nm laser radiation at all irradiances (Figs. 5-7, 5 8, 5-9 5 10)

Silver emission with a 532 nm laser

The time resolved emission spectra of silver are shown in Figures 5 11, 5 12 5 13 5 14 and 5-15 The prominent resonance spectral line observed is 328 068 nm Similar to Cu self reversal is evident throughout the duration of the plasma. At the lowest irradiance (Fig 5-11), the resonance line is sustained until 2.4 µs. The resonance line disappears from the irradiance of 4 7 GW/cm^2 at 3 4 µs (Fig 5-12) At the three highest irradiances (Figs. 5-13 5 14 and 5 15) the resonance line is still visible at the longest delay measured At the highest irradiance, the line is fairly strong at the last measured delay, 3 4 µs. (Fig 5 15)

Silver emission with a 1064 nm laser

Silver emission with a 1064 nm laser follows the emission observed with a 532 nm laser quite closely (Figs. 5 16, 5 17 5 18, 5-19 5 20). At the lowest irradiance (Fig 5 16) the silver resonance line evolves quickly, reaching peak emission at 0.2 µs and vanishing from the spectrum at 2.4 μs. The resonance line at the next irradiance (4.7 GW/cm^2) disappears from the spectrum at 2.4 μs (Fig. 5-17). At the intermediate irradiance of 6.8 GW/cm^2 (Fig. 5-18) the spectral line vanishes from the spectrum at 3.4 μs. Figures 5-19 and 5-20 show that the resonance line is still present at 3.4 μs for laser irradiances of 11 and 21 GW/cm^2.

Gold emission with a 532 nm laser

The resonance line studied for gold was 267.595 nm. As with Cu and Ag, this line is self reversed throughout the duration of the plasma. At the lowest laser irradiance, the resonance line disappears from the spectrum at 1.0 μs (Fig. 5-21). At 4.7 GW/cm^2 the resonance line is present until 2.4 μs (Fig. 5-22). At the three highest laser irradiances (Figs. 5-23, 5-24, 5-25) the resonance line remained in the spectra at the largest delay time of 3.4 μs.

Gold emission with a 1064 nm laser

Figures 5-26, 5-27, 5-28, 5-29 and 5-30 show the time-resolved emission spectra for gold. The resonance lines at the two lowest irradiances (Figs. 5-26 and 5-27) disappear from the spectrum at 1.0 μs. At 6.7 and 11 GW/cm^2 (Figs. 5-28 and 5-29), the resonance line disappears by 3.4 μs. Just as for the 532 nm excitation, the resonance line formed at the highest irradiance is still present at 3.4 μs.

Silicon emission with a 532 nm laser

The resonance line studied for silicon was 251.432 nm. In the same spectral window, several strong non resonance lines were visible at 250.690 nm, 251.611 nm, 251.921 nm, 252.411 nm and 252.851 nm. At a delay of –0.1 μs several self-reversed lines are observed for the irradiances in Figures 5-33, 5-34 and 5-35. These lines are very broad and hard to distinguish from one another. No significant lines are observed for the two lowest irradiances at any delay.

The spectral line widths reduce in Figures 5.33, 5-34 and 5.35 throughout the duration of the plasma. The lines remain self-reversed. At 1.6 µs, the spectral lines observed at a laser irradiance of 6.8 GW/cm^2 disappear. The spectral lines present at the two highest laser irradiances persist until 3.4 µs.

Silicon emission with a 1064 nm laser

At the lowest irradiances, the spectra collected at 1064 are very different from that collected at 532 nm. Spectral lines are present at 2.3 and 4.7 GW/cm^2. The spectral lines at the lowest laser irradiance begin to form at ~0.1 µs and do not disappear until 1.6 µs (Fig. 5.36). In addition, the peaks at an irradiance of 4.7 GW/cm^2 do not disappear from the spectrum until 2.4 µs (Fig. 5.37). Figure 5.38 shows that the spectral lines formed at 6.8 GW/cm^2 irradiance disappear at 3.4 µs. At the longest delay time studied, resonance lines are still present at 11 and 21 GW/cm^2.

Conclusion

Studies of the emission spectra of the laser induced plasma revealed that laser irradiance and laser wavelength affect laser ablation and plasma formation. Several general observations were drawn from the collected emission spectra with respect to varying laser conditions.

- Self reversal of the resonance emission lines was observed at both laser wavelengths.
- Emission with 1064 nm laser radiation was sustained longer than emission with 532 nm radiation.
- The spectral line evolves quickly at lower irradiances.

For all laser irradiances, self reversed resonance spectral lines were observed. Even at the lowest laser irradiance, which is near the breakdown threshold (see Chapter 7), self reversal was present. Self reversed resonance lines suggest that temperature gradients exist within the plasma. Unexcited atoms contained within a cooler region of the plasma absorb radiation emitted from excited atoms within the center of the plasma. The self-absorption results in a dip in the center of the resonance emission line (see Chapter 2).

In general, the emission lines observed with 1064 laser radiation remained for a longer time than the emission lines observed with 532 nm laser radiation. The duration of the emission lines was evidence of plasma shielding (57). Plasma shielding is the result of absorption of laser radiation by the plasma. The absorption is proportional to the square of the laser wavelength. Therefore, atoms within a plasma generated at 1064 nm will absorb laser radiation 4 times more than atoms generated at 532 nm (57).

The spectral lines observed at lower laser irradiances evolved quickly. The emission was present at the earliest delays and disappeared quickly. At the lowest irradiances, the laser energy absorbed at the sample surface was consumed during the heating, melting and vaporization mechanisms of plasma formation (34). Little energy was left to contribute to the propagation of the plasma and further excitation of atomic species within the plasma. Therefore, excited atoms within the plasma relaxed to the ground state and the plasma was short-lived.

At higher laser irradiances, the emission lines developed over a longer period of time. Spectral lines formed at shorter delays and continued to persist for longer delay times. At higher laser irradiances, only a fraction of the laser energy is used in the heating, melting and vaporization mechanisms. Therefore, plasmas formed at higher irradiances continue propagate throughout the duration of the laser pulse. Laser energy is available to interact with atoms in the plasma, resulting in prolonged emission.

Table 5-1 Laser powers measured for each study and the attenuated irradiances used.

λ_{laser} (nm)	Emission	P_{avg}^{a} (W)	ϕ* (GW/cm^2)	ϕ_A** (GW/cm^2)	ϕ_B** (GW/cm^2)	ϕ_C** (GW/cm^2)	ϕ_D** (GW/cm^2)	ϕ_E** (GW/cm^2)
532	Resonance	0.036	26	2.3	4.7	6.8	11	21
	Non resonance	0.034	25	2.3	4.5	6.6	13	20
1064	Resonance	0.58	420	2.2	3.9	6.6	11	18
	Non resonance	0.58	420	2.2	3.9	6.6	11	18

^{a}There was a 5% uncertainty in the measurement.

* $\varphi = \frac{P_{avg}}{\tau f A}$ where τ= 12.2 ns f =10 s^{-1} and A=1.13E-5 cm^2

** Attenuated irradiances for comparative studies, attenuated with required filters for visible and IR region, see Chapter 4 for description

Table 5-2. Wavelengths for resonance lines of Cu, Ag, Au and Si

Element	Wavelength^a (nm)	Energy Levels K	gA 10^8/s	gf
Cu	324.754	0 – 30784	4.1	0.64
	327.396	0 – 30535	1.9	0.31
Ag	328.068	0 – 30473	3.3	0.53
Au	267.595	0 – 37359	1.1	0.12
Si	250.690*	77 – 39955	6.3	0.60
	251.432	0 – 39760	5.7	0.54
	251.611*	223 – 39955	13	1.3
	251.921*	77 – 39760	4.3	0.41
	252.411*	77 – 39683	8.4	0.80
	252.851*	223 – 39760	7.1	0.68

^{a}Values taken from NBS Monograph 53 (58)

*Though not resonance lines, these lines are very strong and self-reversed in the spectra.

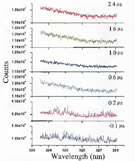

Figure 5-1 Time resolved emission spectra for copper between 323 and 328 nm at a laser excitation of 532 nm and irradiance of 2.3 GW/cm^2

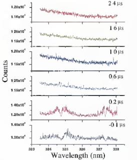

Figure 5.2 Time-resolved emission spectra for copper between 323 and 328 nm at a laser excitation of 532 nm and irradiance of 4.7 GW/cm^2

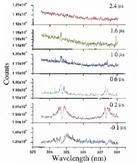

Figure 5-3 Time resolved emission spectra for copper between 323 and 328 nm at a laser excitation of 532 nm and irradiance of 6.8 GW/cm^2

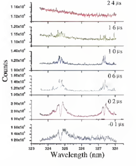

Figure 5-4 Time-resolved emission spectra for copper between 323 and 328 nm at a laser excitation of 532 nm and irradiance of 11 GW/cm^2

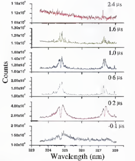

Figure 5.5 Time resolved emission spectra for copper between 323 and 328 nm at a laser excitation of 532 nm and irradiance of 21 GW/cm^2

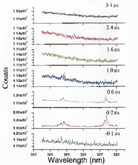

Figure 5-6 Time resolved emission spectra for copper between 323 and 328 nm at a laser excitation of 1064 nm and irradiance of 2.3 GW/cm^2

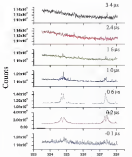

Figure 5-7 Time resolved emission spectra for copper between 323 and 328 nm at a laser excitation of 1064 nm and irradiance of 4.7 GW/cm^2

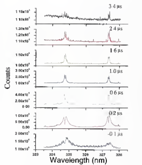

Figure 5-8 Time-resolved emission spectra for copper between 323 and 328 nm at a laser excitation of 1064 nm and irradiance of 6.8 GW/cm^2

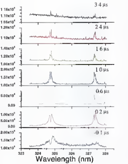

Figure 5-9 Time resolved emission spectra for copper between 323 and 328 nm at a laser excitation of 1064 nm and irradiance of 11 GW/cm^2

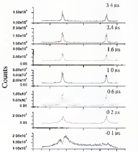

Figure 5-10 Time-resolved emission spectra for copper between 323 and 328 nm at a laser excitation of 1064 nm and irradiance of 21 GW/cm^2

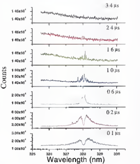

Figure 5.11. Time-resolved emission spectra for silver between 325 and 330 nm at a laser excitation of 532 nm and irradiance of 2.3 GW/cm^2

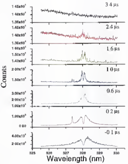

Figure 5-12 Time-resolved emission spectra for silver between 325 and 330 nm at a laser excitation of 532 nm and irradiance of 4 7 GW/cm^2

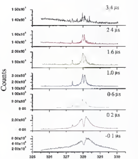

Figure 5-13. Time-resolved emission spectra for silver between 325 and 330 nm at a laser excitation of 532 nm and irradiance of 6.8 GW/cm^2

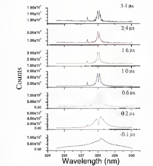

Figure 5-14 Time-resolved emission spectra for silver between 325 and 330 nm at a laser excitation of 532 nm and irradiance of 11 GW/cm^2

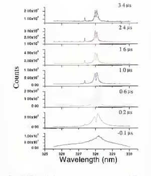

Figure 5-15 Time-resolved emission spectra for silver between 325 and 330 nm at a laser excitation of 532 nm and irradiance of 21 GW/cm^2

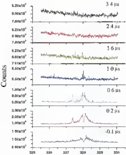

Figure 5.16 Time-resolved emission spectra for silver between 325 and 330 nm at a laser excitation of 1064 nm and irradiance of 2.3 GW/cm^2

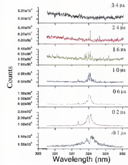

Figure 5-17 Time resolved emission spectra for silver between 325 and 330 nm at a laser excitation of 1064 nm and irradiance of 4 7 GW/cm^2

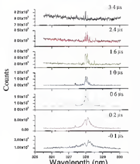

Figure 5-18 Time-resolved emission spectra for silver between 325 and 330 nm at a laser excitation of 1064 nm and irradiance of 6.8 GW/cm^2

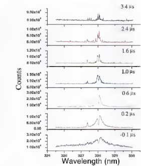

Figure 5.19 Time resolved emission spectra for silver between 325 and 330 nm at a laser excitation of 1064 nm and irradiance of 11 GW/cm^2

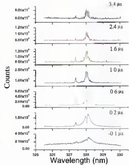

Figure 5.20 Time-resolved emission spectra for silver between 325 and 330 nm at a laser excitation of 1064 nm and irradiance of 21 GW/cm^2

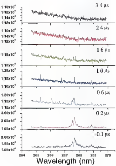

Figure 5-21–Time-resolved emission spectra for gold between 264 and 270 nm at a laser excitation of 532 nm and irradiance of 2.3 GW/cm^2

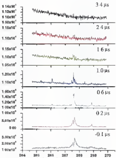

Figure 5.22. Time-resolved emission spectra for gold between 264 and 270 nm at a laser excitation of 532 nm and irradiance of 4.7 GW/cm²

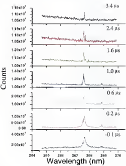

Figure 5.23 Time resolved emission spectra for gold between 264 and 270 nm at a laser excitation of 532 nm and irradiance of 6.0 GW/cm^2

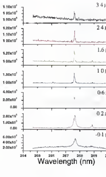

Figure 5-24 Time-resolved emission spectra for gold between 264 and 270 nm at a laser excitation of 532 nm and irradiance of 11 GW/cm^2

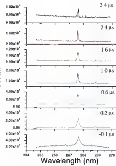

Figure 5.25 Time-resolved emission spectra for gold between 264 and 270 nm at a laser excitation of 532 nm and irradiance of 21 GW/cm^2

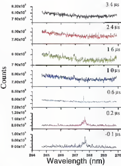

Figure 5.26 Time-resolved emission spectra for gold between 264 and 270 nm at a laser excitation of 1064 nm and irradiance of 2.3 GW/cm^2

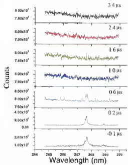

Figure 5 27 Time resolved emission spectra for gold between 264 and 270 nm at a laser excitation of 1064 nm and irradiance of 4 7 GW/cm^2

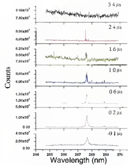

Figure 5-28 Time resolved emission spectra for gold between 264 and 270 nm at a laser excitation of 1064 nm and irradiance of 6.8 GW/cm^2

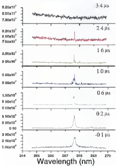

Figure 5.29 Time-resolved emission spectra for gold between 264 and 270 nm at a laser excitation of 1064 nm and irradiance of 11 GW/cm^2

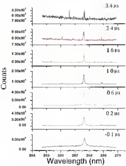

Figure 5.30 Time resolved emission spectra for gold between 264 and 270 nm at a laser excitation of 1064 nm and irradiance of 21 GW/cm²

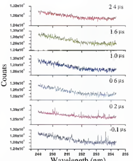

Figure 5-31 Time-resolved emission spectra for silicon between 249 and 254 nm at a laser excitation of 532 nm and irradiance of 2.3 GW/cm^2

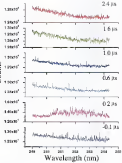

Figure 5.32. Time resolved emission spectra for silicon between 249 and 254 nm at a laser excitation of 532 nm and irradiance of 4.7 GW/cm^2

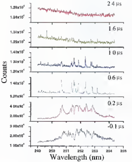

Figure 5.33 Time resolved emission spectra for silicon between 249 and 254 nm at a laser excitation of 532 nm and irradiance of 6.8 GW/cm^2

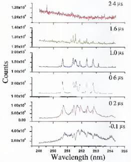

Figure 5.34 Time resolved emission spectra for silicon between 249 and 254 nm at a laser excitation of 532 nm and irradiance of 11 GW/cm^2

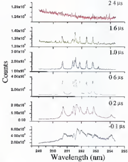

Figure 5-35 Time resolved emission spectra for silicon between 249 and 254 nm at a laser excitation of 532 nm and irradiance of 21 GW/cm^2

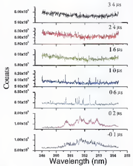

Figure 5.36 Time-resolved emission spectra for silicon between 249 and 254 nm at a laser excitation of 1064 nm and irradiance of 2.3 GW/cm^2

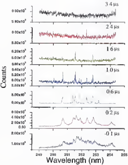

Figure 5.37 Time-resolved emission spectra for silicon between 249 and 254 nm at a laser excitation of 1064 nm and irradiance of 4.7 GW/cm^2

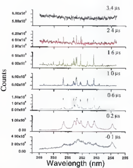

Figure 5.38 Time-resolved emission spectra for silicon between 249 and 254 nm at a laser excitation of 1064 nm and irradiance of 6.8 GW/cm^2

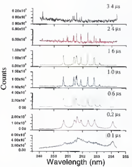

Figure 5.39 Time resolved emission spectra for silicon between 249 and 254 nm at a laser excitation of 1064 nm and irradiance of 11 GW/cm^2

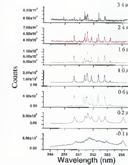

Figure 5-40. Time resolved emission spectra for silicon between 249 and 254 nm at a laser excitation of 1064 nm and irradiance of 21 GW/cm^2

CHAPTER 6

STUDY OF NON-RESONANCE EMISSION OF Cu, Ag, Au AND Si

Introduction

This is the second of two chapters that focus on time-resolved in a laser generated plasma. The aim of this chapter is to examine the influence of laser irradiance and laser wavelength on the spectral emission of the non-resonance lines of copper, silver gold and silicon

Experiment

The experimental set-up is described in Chapter 4. Similar to the experiment in Chapter 5, each sample was ablated using 532 nm and 1064 nm laser radiation at five different irradiances. Time-resolved emission from each sample was collected at the several gate delays with a gate width of 0.3 µs. The delays intervals were -0.1 µs, 0.2, 0.6 µs, 1.0 µs, 1.6 µs, 2.4 µs, 3.4 µs. Table 6-1 lists the spectral line studied for each metal.

Results and Discussion

Copper emission with a 532 nm laser

Figures 6-1, 6-2, 6-3, 6-4 and 6-5 show the time-resolved emission spectra for copper at five increasing laser irradiances with a 532 nm laser. The prominent spectral line in the window of interest was 249.489 nm. At –0.1 µs, the spectral line emerges from the continuum background. The line continues to develop at all irradiances through

0.6 µs. At 0.6 µs, the spectral line has disappeared from the spectrum at the lowest laser irradiance (Fig. 6-1). The spectral line finally disappears from the spectrum of the highest laser irradiances at the delay time of 3.4 µs (Fig. 6-5).

Copper emission with a 1064 nm laser

The copper target was also sampled at 1064 nm. Figures 6-6, 6-7, 6-8, 6-9 and 6-10 show the time-resolved emission spectra for copper at the five laser irradiances. At the earliest delay time, the spectral line begins to emerge from the background. By 0.2 µs the spectral line is present in every spectrum. At 2.3 GW/cm^2, the spectral line disappears from the spectrum by 1.0 µs. By 2.4 µs, the spectral line has disappeared from the spectrum at the laser irradiance of 21 GW/cm^2.

Silver emission with a 532 nm laser

The time resolved emission spectra of silver with a 532 nm laser are shown in Figures 6-11, 6-12, 6-13, 6-14 and 6-15. The spectral line of interest is 243.779 nm. The line is not visible at the lowest irradiance. At 4.7 GW/cm^2, the emission peak appears in the spectrum at 0.2 µs and disappears at 1.6 µs. At higher laser irradiances, the spectral line is present until 2.4 µs at 6.8 GW/cm^2 and 3.4 µs at 11 GW/cm^2 and 21 GW/cm^2.

Silver emission with a 1064 nm laser

The spectral line profile with a 1064 nm laser is very similar to that of a 532 nm laser (Figs. 6-16, 6-17, 6-18, 6-19, 6-20). At the early delay of 0.2 µs, the peak of interest is hidden within the continuum background. At 2.3 GW/cm^2, the spectral line disappears at a delay time of 1.0 µs. At 1.6 µs, the spectral line vanishes with laser irradiances of 4.7 and 6.8 GW/cm^2. The spectral line at the highest laser irradiance is still present at the longest delay time studied, 3.4 µs.

Gold emission with a 532 nm laser

The spectral line studied for gold was 274.826 nm. The time-resolved spectra at the 5 laser irradiances can be found in Figures 5-26, 5-27, 5-28, 5-29 and 5-30. At the earliest delay of –0.1 µs, an intense, broad line emerges from a continuum background at all the laser irradiances. At 1.0 µs, the spectral line has disappeared from the spectrum of the lowest irradiance, but is still visible in the spectra of all the other laser irradiances. At a delay of 1.6 µs, the spectral line at a laser irradiance of 4.7 GW/cm^2 vanishes. By 3.4 µs, the spectral line has disappeared from the spectra at all irradiances.

Gold emission with a 1064 nm laser

Figures 6-26, 6-27, 6-28, 6-29 and 6-30 show the time-resolved emission spectra for gold. The observed spectral line is very similar to the line observed at 532 nm. At –0.1 µs, the spectral line is distinguished from the background. At 1.6 µs, the spectral line disappears from all spectra at laser irradiances between 2.3 and 6.8 GW/ cm^2. At the laser irradiances of 11 to 21 GW/cm^2, the spectral line disappears by 3.4 µs.

Silicon emission with a 532 nm laser

The spectral line studied for silicon was 288.160 nm. Figures 6-31, 6-32, 6-33, 6-34 and 6-35 show the time-resolved spectra at the five laser irradiances. At a delay of –0.1 µs, the spectral line is very broad at all laser irradiances. At the lowest irradiance, the line never really develops and disappears into the noise by 0.2 µs. At 1.6 µs, the emission line disappears at a laser irradiance of 4.7 GW/cm^2. At laser irradiances of 6.8 to 21 GW/cm^2, the line decreases in intensity and it disappears from all spectra at 3.4 µs.

Silicon emission with a 1064 nm laser

The silicon spectral lines observed in Figures 6-36, 6-37, 6-38, 6-39 and 6-40 are quite broad at the earliest delay times. Unlike Figure 6-31, the spectral lines at the laser irradiance of 2.3 to 4.7 GW/cm^2 begin to form at ~0.1 µs. The lines do not disappear from the spectrum until 1.6 µs (Figs. 6-36 and 6-37). Figures 6-39 and 6-40 show that the resonance lines are still visible at the longest delay time studied.

Conclusion

Similar to the previous studies (see chapter 5), several general observations were drawn from the emission spectra.

- A continuum background was present at the earliest delay times.
- Emission with 1064 nm laser radiation was sustained longer than emission with 532 nm laser radiation.

The spectral lines studied in the experiment all had very similar development. The line emerged from a continuum background as a broad peak. At the earliest delay times, the continuum background can be attributed to Bremsstrahlung radiation (59). Within the plasma, charged particles slow and stop resulting in the emission of continuum radiation (29). As time passes, the continuum background decreases due to plasma propagation, cooling and recombination (56).

The aim of chapters 5 and 6 was to use spectroscopic methods to understand the mechanisms occurring during laser ablation and plasma formation. The emission spectra of several elements were studied at various delays using two laser wavelengths and 5 laser irradiances. The studies revealed that plasma shielding affects the efficiency of laser energy delivered to the target. Spectral analysis presented an improved understanding of the processes that occur within the plasmas.

Table 6-1 Spectral lines observed for copper, silver, gold and silicon.

Element	Wavelength[a] (nm)	Energy Levels K (cm^{-1})	gA 10^8/sec	gf
Cu*	249.489	30810 – 70815	[b]	-[b]
Ag	243.779	39164 – 80172	13	1.2
Au	274.826	9161 – 45537	3.8	0.43
Si	288.160	6299 – 40992	15	1.9

[a]Values taken from NBS Monograph 53 (58)

*Values taken from Striganov (61).

[b]Values not available.

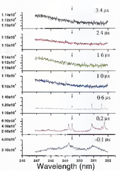

Figure 6-1 Time-resolved emission spectra for copper between 247 and 252 nm at a laser excitation of 532 nm and irradiance of 2.3 GW/cm^2

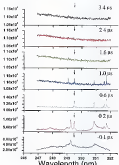

Figure 6-2. Time resolved emission spectra for copper between 247 and 252 nm at a laser excitation of 532 nm and irradiance of 4.7 GW/cm^2

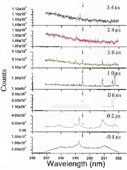

Figure 6-3 Time resolved emission spectra for copper between 247 and 252 nm at a laser excitation of 532 nm and irradiance of 6.8 GW/cm^2

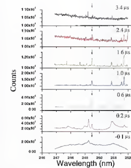

Figure 6-4 Time-resolved emission spectra for copper between 247 and 252 nm at a laser excitation of 532 nm and irradiance of 11 GW/cm^2

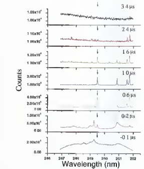

Figure 6-5 Time-resolved emission spectra for copper between 247 and 252 nm at a laser excitation of 532 nm and irradiance of 21 GW/cm^2

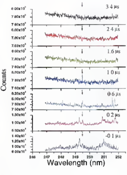

Figure 6-6 Time resolved emission spectra for copper between 247 and 252 nm at a laser excitation of 1064 nm and irradiance of 2.3 GW/cm^2

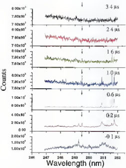

Figure 6-7 Time-resolved emission spectra for copper between 247 and 252 nm at a laser excitation of 1064 nm and irradiance of 4.7 GW/cm²

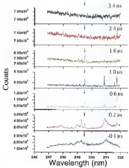

Figure 6-8. Time resolved emission spectra for copper between 247 and 252 nm at a laser excitation of 1064 nm and irradiance of 6.8 GW/cm^2

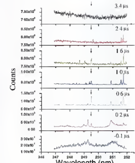

Figure 6-9 Time-resolved emission spectra for copper between 247 and 252 nm at a laser excitation of 1064 nm and irradiance of 11 GW/cm^2

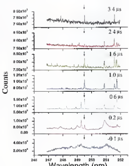

Figure 6-10 Time-resolved emission spectra for copper between 247 and 252 nm at a laser excitation of 1064 nm and irradiance of 21 GW/cm^2

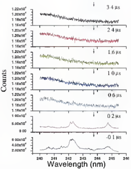

Figure 6-11 Time resolved emission spectra for silver between 239 and 244 nm at a laser excitation of 532 nm and irradiance of 2.3 GW/cm^2

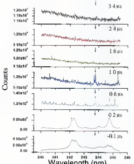

Figure 6-12 Time-resolved emission spectra for silver between 239 and 244 nm at a laser excitation of 532 nm and irradiance of 4.7 GW/cm^2

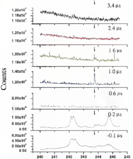

Figure 6-13 Time-resolved emission spectra for silver between 239 and 244 nm at a laser excitation of 532 nm and irradiance of 6.8 GW/cm^2

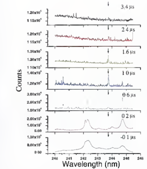

Figure 6-14 Time resolved emission spectra for silver between 239 and 244 nm at a laser excitation of 532 nm and irradiance of 1.1 GW/cm^2

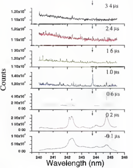

Figure 6-15. Time resolved emission spectra for silver between 239 and 244 nm at a laser excitation of 532 nm and irradiance of 21 GW/cm^2

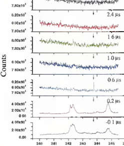

Figure 6-16 Time-resolved emission spectra for silver between 239 and 244 nm at a laser excitation of 1064 nm and irradiance of 2.3 GW/cm²

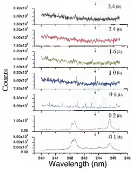

Figure 6-17 Time resolved emission spectra for silver between 239 and 244 nm at a laser excitation of 1064 nm and irradiance of 4.7 GW/cm^2

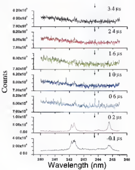

Figure 6-18 Time-resolved emission spectra for silver between 239 and 244 nm at a laser excitation of 1064 nm and irradiance of 6.8 GW/cm^2

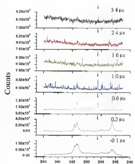

Figure 6-19 Time-resolved emission spectra for silver between 239 and 244 nm at a laser excitation of 1064 nm and irradiance of 11 GW/cm²

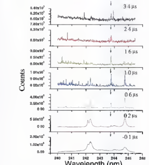

Figure 6-20 Time-resolved emission spectra for silver between 239 and 244 nm at a laser excitation of 1064 nm and irradiance of 21 GW/cm^2

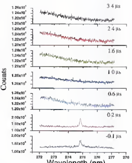

Figure 6-21 Time-resolved emission spectra for gold between 272 and 277 nm at a laser excitation of 532 nm and irradiance of 2.3 GW/cm^2

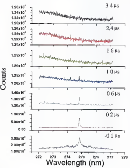

Figure 6-22. Time-resolved emission spectra for gold between 272 and 277 nm at a laser excitation of 532 nm and irradiance of 4.7 GW/cm^2

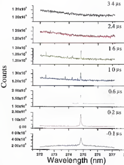

Figure 6-23 Time resolved emission spectra for gold between 272 and 277 nm at a laser excitation of 532 nm and irradiance of 6.8 GW/cm^2

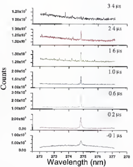

Figure 6-24 Time-resolved emission spectra for gold between 272 and 277 nm at a laser excitation of 532 nm and irradiance of 11 GW/cm^2

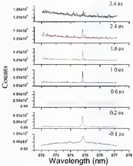

Figure 6-25 Time resolved emission spectra for gold between 272 and 277 nm at a laser excitation of 532 nm and irradiance of 21 GW/cm

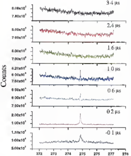

Figure 6-26 Time resolved emission spectra for gold between 272 and 277 nm at a laser excitation of 1064 nm and irradiance of 2 3 GW/cm²

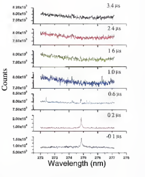

Figure 6-27 Time-resolved emission spectra for gold between 272 and 277 nm at a laser excitation of 1064 nm and irradiance of 4.7 GW/cm^2

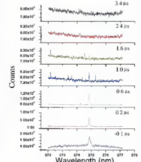

Figure 6-28 Time-resolved emission spectra for gold between 272 and 277 nm at a laser excitation of 1064 nm and irradiance of 6.8 GW/cm^2

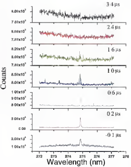

Figure 6-29 Time resolved emission spectra for gold between 272 and 277 nm at a laser excitation of 1064 nm and irradiance of 11 GW/cm^2

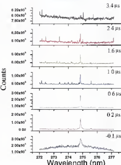

Figure 6-30 Time-resolved emission spectra for gold between 272 and 277 nm at a laser excitation of 1064 nm and irradiance of 2.1 GW/cm^2

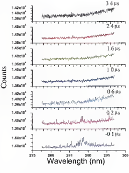

Figure 6-31 Time-resolved emission spectra for silicon between 278 and 298 nm at a laser excitation of 532 nm and irradiance of 2.3 GW/cm^2

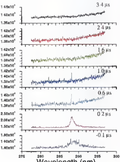

Figure 6-32 Time-resolved emission spectra for silicon between 278 and 298 nm at a laser excitation of 532 nm and irradiance of 4.7 GW/cm^2

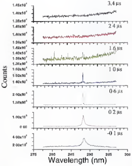

Figure 6-33 Time-resolved emission spectra for silicon between 278 and 298 nm at a laser excitation of 532 nm and irradiance of 6.8 GW/cm^2

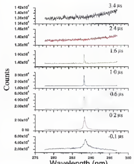

Figure 6-34 Time resolved emission spectra for silicon between 278 and 298 nm at a laser excitation of 532 nm and irradiance of 11 GW/cm^2

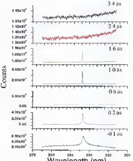

Figure 6-35 Time resolved emission spectra for silicon between 278 and 298 nm at a laser excitation of 532 nm and irradiance of 21 GW/cm^2

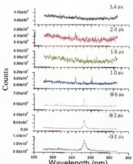

Figure 6-36 Time-resolved emission spectra for silicon between 278 and 298 nm at a laser excitation of 1064 nm and irradiance of 2.3 GW/cm^2

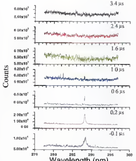

Figure 6-37 Time-resolved emission spectra for silicon between 278 and 298 nm at a laser excitation of 1064 nm and irradiance of 4.7 GW/cm^2

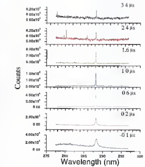

Figure 6-38 Time resolved emission spectra for silicon between 278 and 298 nm at a laser excitation of 1064 nm and irradiance of 6.8 GW/cm^2

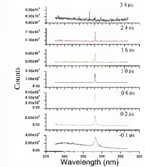

Figure 6-39 Time-resolved emission spectra for silicon between 278 and 298 nm at a laser excitation of 1064 nm and irradiance of 11 GW/cm^2

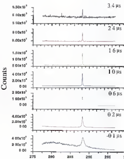

Figure 6-40 Time resolved emission spectra for silicon between 278 and 298 nm at a laser excitation of 1064 nm and irradiance of 21 GW/cm^2

CHAPTER 7
EFFECTS OF IRRADIANCE AND LASER WAVELENGTH ON THE ABLATION Cu, Ag, Au AND Si

Introduction

Lasers are used in several mass removal procedures such as pulsed-laser thin-film deposition, laser machining and microfabrication. Mass removal can vary with laser irradiance as well as laser wavelength. Consequently, atom concentration within the plasma is affected. Spectral emission from the plasma is commonly monitored to determine the effects of laser irradiance and wavelength (62). In this chapter, the laser ablation and spectral emission of copper, silver, gold and silicon is studied with respect to laser irradiance and laser wavelength.

Experiment

Copper, silver, gold and silicon were prepared as explained in Chapter 4. For each sample, several steps were followed for data collection, manipulation and analysis. First, single-shot spectra were collected at 5 laser irradiances for laser wavelengths of 532 nm and 1064 nm (See Table 5.2 for laser irradiances). At each laser irradiance, 5 spectra were collected at delay times of –0.1, 0.2, 0.6, 1.0, 1.6, 2.4 and 3.4 µs with a gate width of 0.3 µs. Therefore, 200 data files existed for each sample at both laser wavelengths.

Data collection software was used to save each spectrum as a binary file, unreadable by any other program. For data analysis, it was necessary to write a computer program, which converted the binary files to a form of ASCII. The written program opened each binary file and converted it to comma-delimited text. Next, the program prompted the user to input the pixel of the emission peak as well as the pixels of the background on either side of the peak. The background was averaged and subtracted from the peak of interest. The output signal was placed in a file, which was appended as every spectrum was analyzed.

Each crater formed from laser ablation was analyzed using a profilometer (Vecco Instruments Dektak 3030, Plainview, NY). The profilometer tip was made of carbon fiber and had a tip size of 5 µm. The tip was scanned across the sample surface. A typical scan can be seen in Figure 7-1. The depth and width of the crater were taken from each scan and averaged over 5 scans. The average depth and width of the ablation craters at each laser irradiance are shown in Table 7-1.

Using a cone approximation, the volume ablated, $V_{ablated}$ (cm^3), was calculated (Eq. 7-1). The radius of each crater is r (cm) and the height is h (cm).

(Eq. 7-1) $$V_{ablated} = \frac{\pi r^2 h}{3}$$

The average ablated mass ($m_{ablated}$ (g)) was calculated from equation 7-2. The density, ρ (g/cm^3), is element specific. The average ablated volume and the average ablated mass for each sample is shown in Table 7-2.

(Eq. 7-2) $$m_{ablated} = V_{ablated}\rho$$

Results and Discussion

Determination of optimum delay and gate

Prior to studying the effects of laser irradiance and wavelength, the optimum gate delay and gate width were determined. A plot of the signal-to-noise ratio (S/N) versus the delay time shows the temporal developments of the S/N. To construct plots for each sample under the experimental conditions the S/N ratio was calculated for each emission peak studied The noise was calculated from the standard deviation in the background surrounding the emission peak. The S/N was averaged over 5 spectra.

The plots obtained for each sample for the experimental conditions are shown in Figures 7-2, 7-3, 7-4 and 7-5 At the lower laser irradiances, the S/N ratio rises and falls over a short period of time (<1 µs) For a discussion on the formation of emission lines in the plasma, please see chapters 5 and 6.

Each S/N curve has approximately a triangular shape The optimum gate delay and width were determined by approximating the base of the triangular shape. The gate delays and gate widths, determined from the plots, are tabulated in Table 7-3

S/N versus laser irradiance

Five emission spectra were collected at each laser irradiance using the optimum gate delays and gate widths. Figures 7-6 and 7-7 show the S/N versus laser irradiance at laser wavelengths of 532 nm and 1064 nm At both laser wavelengths, the S/N increases sharply at low irradiances At irradiances larger than 11 GW/cm^2 the S/N reaches a saturated level The leveling phenomenon has been observed by previous researchers (60 63 64). Researchers determined that the phenomenon is caused by the dependence of the plasma temperature and electron number density on the laser irradiance. Calculations of plasma temperature (T_e) and electron number density (n_e) found that T_e and n_e increase with laser irradiance to a critical irradiance. The increase follows a power law ($n_e \propto E^{0.24}$, $T_e \propto E^{0.54}$) (60) The power law changes beyond the critical point, where $n_e \propto E^{0.45}$ and $T_e \propto E^{0.45}$ Further studies on the change of the electron density in the plasma revealed that the ratio of ions to atoms (n_i/n_a) within the plasma saturated at the critical irradiance (60). In figures 7-6 and 7-7, the leveling of the S/N can be attributed to the saturation phenomenon.

The laser wavelength also has an effect on the absolute value of the S/N ratio. At 532 nm, the S/N ratios of copper, silver and gold are 50%, 25% and 13% greater than the S/N ratios at 1064 nm. The S/N ratio for silicon at 532 nm is 50% greater than the S/N ratio at 1064 nm.

Crater volume versus laser irradiance

Measurements of crater volume versus laser irradiance are plotted in figure 7-8. The actual values of the crater volumes are shown in Table 7.2. At 1064 nm, the ablation volume of Au could not be measured. The craters created were too small to be measured by the profilometer. The tip could not enter the crater. Atomic Force Microscopy (AFM) was also used to measure the gold craters, but the AFM tip had trouble overcoming hydrodynamic forces from polar contaminants on the surface. Another technique used to measure the Au crater depth was optical microscopy. Theoretically, the depth of the crater could be determined using a calibrated focus. The microscope was focused inside the crater and outside of the crater. The change in the focus position should give the crater depth. Unfortunately, the adjustment of the focus was not fine enough to determine a depth smaller than 1.0 µm. It can be assumed that the Au craters at 1064 nm are smaller than any other crater studied. The smallest crater measured has a volume of 18 μm^3.

The amount of material ablated by the laser varies with laser irradiance. Figure 7-8A shows the effect of laser irradiance on crater volume at a laser wavelength of 532 nm and figure 7-8B shows the effect of irradiance on crater volume at a laser wavelength of

1064 nm. In general, the crater volume increases slowly until the critical point (11 GW/cm^2). The slope of the curve increases past the critical irradiance. Previous researchers discovered that below the critical irradiance, the ablated material accumulates on the target surface. Only a small amount enters the plasma (60). Past the critical irradiance, the material is ejected away from the sample into the plasma.

The volume of material ablated is significantly different at 532nm from 1064 nm. For copper and silver, the volume ablated is much greater at 532 nm than at 1064 nm. Table 7-4 shows the percent change in volume ablated between 532 nm and 1064 nm before and after the critical point. Though the gold craters at 1064 nm could not be measured, it can be assumed that gold follows a similar trend.

A sample property, which may be responsible for the increase in ablated volume at 532 nm is absorptivity. When light strikes an opaque sample, the light is either reflected or absorbed. Absorptance is defined as the fraction light that is absorbed at the surface of a sample. Each sample has a unique absorptance for the wavelength of the incident light. Copper, silver and gold have absorptances of 5.5%, 3% and 5% at 532 nm (65). At 1064 nm, their absorptances are roughly half that at 532 nm: 2.5%, 1.8% and 2.2%. Therefore, the laser energy at 1064 nm is not absorbed as effectively as at 532 nm. This change is indicated in the lower ablation volume at 1064 nm.

In sharp contrast, the silicon ablation volume does not increase at shorter wavelengths. A decrease of 18% is found before the critical irradiance and a decrease of 8% is found after the critical irradiance. The percent decrease is within the error bars for the ablation volume. Therefore, it can be stated that at 532 nm, the silicon ablation volume is relatively the same as the silicon ablation volume at 1064 nm. Silicon has absorptances of 60% at 532 nm and 70% at 1064 nm (66) The constant ablation volume is reflected in the similar absorptances of silicon at both wavelengths

Signal versus crater volume

The signal emitted from the plasma is dependent on the atom concentration within the plasma (34) Therefore, it is useful to relate the signal to the volume of sample ablated. It has been previously discussed that the crater volume increases rapidly at lower irradiances and plateaus at higher irradiances. Plots of signal versus volume ablated are shown in Figures 7-9, 7-10, 7-11 and 7-12

With respect to wavelength, the signal is considerably larger at 532 nm than at 1064 nm for copper, silver and gold Kim and coworkers found that the excitation temperatures within the plasma are higher at shorter wavelengths (67) At higher temperatures, more atoms within the plasma will be excited to higher energy states The increase in excited atoms causes an increase in the pure signal detected.

Figure 7-12A and 7-12B show the relationship between silicon signal and crater volume ablated at 532 nm and 1064 nm respectively At both wavelengths, the silicon signal is relatively the same at similar crater volumes

Determination of breakdown thresholds

Using the equation proposed by Moenke-Blankenburg (38) (see Chapter 2), the breakdown thresholds were calculated for each metal Table 7-4 lists the calculated thresholds as well as the constants used in the calculation The calculated thresholds are one order of magnitude smaller than the smallest laser irradiances used in the experiments. Lower irradiances were investigated but no visible breakdown was observed

As described in chapter 3, the breakdown threshold can also be determined experimentally. Researchers determined the breakdown threshold as the minimum irradiance needed to detect an emission signal (50). The limit of detection is defined as a S/N ratio of 3. Therefore, the breakdown threshold is the laser irradiance at which a S/N ratio of 3 is obtained. Other researchers have extrapolated the breakdown threshold from the ablation volume (49). Using plots of ablation volume versus irradiance, the breakdown threshold was extrapolated at the ablation volume equal to 0.

From the plots in figures 7-6, 7-7 and 7-8, the experimental breakdown thresholds were estimated using the two methods described above. Table 7-5 lists the experimental values as well as literature values. The experimental values follow similar trends as the literature values with a few exceptions. Using the S/N method at 532 nm, the experimental thresholds compare nicely with the literature values, with the exception of silver. At 532nm, breakdown thresholds determined using the volume-ablated method follow the same trend as the literature, but they are considerably different in value. At 1064 nm, the experimental thresholds do not follow the literature trends. Unfortunately, no literature values were found for silicon at the wavelengths used in this experiment. The two values found at 248 nm and 266 nm are quite different and are not useful for comparison.

The experimental thresholds can also be compared to the theoretical breakdown thresholds. The S/N method determines values that are closest to the theoretical thresholds. For copper, the value of 0.4 GW/cm^2 (found using the S/N method) is the same as the theoretical threshold of 0.407 GW/cm^2.

With respect to the volume ablated (Table 7-2), copper, silver and gold follow the same trend in volume ablated as obtained in calculated breakdown thresholds (Table 7-4). Copper has the highest calculated threshold of 0.407 GW/cm^2 and the lowest ablated volume. Silver and gold have very similar thresholds of 0.296 GW/cm^2 and 0.321 GW/cm^2. Therefore, their ablation volumes are similar in value and considerably higher than copper.

The breakdown threshold of silicon is 0.256 GW/cm^2, which is the lowest of the calculated thresholds. Though silicon has a lower breakdown threshold, it does not have the highest ablation volume. However, because silicon is an optical material, it can not be expected to follow the same trend as copper, silver and gold. A better comparison for silicon would be between other optical materials.

Conclusion

The effects on laser irradiance and laser wavelength on several plasma and crater properties have been discussed. Several trends were observed.

- S/N increased with increasing laser irradiance to a critical point. Past the critical point, the S/N leveled.
- S/N was affected by laser wavelength.
- The ablated crater volumes of Cu, Ag and Au were greater with 532 nm laser radiation than with 1064 nm laser radiation. The ablated crater volumes of Si were similar for both laser wavelengths.

It was found surface absorptance plays a critical role in the S/N and crater volume. For optimum S/N at minimal crater volumes, shorter laser wavelengths should be used. In addition, non-linear measurements were observed in the S/N plots. The plots suggest significant changes in the laser material and laser plasma interactions. Experimental and theoretical thresholds were compared. It was found that the S/N method is the best to determine the breakdown threshold.

Table 7.1 Average crater heights and widths at 5 laser irradiances with 532 and 1064 nm laser wavelengths

Laser Wavelength (nm)	Sample	Irradiance (GW/cm^2)	Crater Depth (nm)	Crater Width (µm)
532	Cu	2.3	387±23	16.4±1.1
		4.7	786±50	23.8±1.9
		6.8	829±80	32.8±3.1
		11	924±131	50.4±2.6
		21	1440±360	56.4±5.7
	Ag	2.3	1176±99	41.6±1.9
		4.7	1264±192	43.4±6.5
		6.8	1681±149	52.0±2.1
		11	1875±238	62.4±3.5
		21	2367±226	69.6±9.0
	Au	2.3	727±174	30.6±1.1
		4.7	1132±298	50.0±5.3
		6.8	1752±779	66.8±12.4
		11	1969±241	72.6±7.8
		21	2516±446	88.8±2.2
	Si	2.3	615±110	43.0±1.7
		4.7	874±68	52.5±0.7
		6.6	969±105	46.7±10.7
		11	942±186	62.7±5.9
		21	913±91	64.3±5.8
1064	Cu	2.3	349±98	14.0±2.6
		4.7	448±109	21.0±0
		6.8	636±109	30.2±1.1
		11	833±101	33.8±1.6
		21	939±140	42.4±1.6
	Ag	2.3	254±126	8.2±1.3
		4.7	479±175	17.6±0.6
		6.6	717±37	22.2±5.0
		11	937±107	30.0±3.4
		21	1451±318	34.0±3.1
	Au*	2.3		
		4.7		
		6.8		
		11		
		21		
	Si	2.3	850±113	29.6±1.9
		4.7	974±124	39.2±5.6
		6.6	1000±68	50.6±1.5
		11	1238±106	54.2±1.7
		21	1122±144	60.4±2.5

*The gold craters at this laser wavelength were not measurable by the techniques available

Table 7-2 Ablated volume for Cu, Ag, Au and Si at 5 laser irradiances with 532 and 1064 nm laser wavelengths.

Laser Wavelength (nm)	Sample	Irradiance (GW/cm^2)	Volume Ablated (μm^3)	Mass Ablated (μg)
532	Cu	2.3	34±4	0.3±0.03
		4.7	116±14	1.0±0.1
		6.8	233±39	2.1±0.3
		11	614±130	5.5±1.1
		21	1210±330	10.8±2.9
	Ag	2.3	532±68	5.6±0.7
		4.7	623±160	6.5±1.7
		6.8	1910±160	12.5±1.6
		11	1910±360	20.0±3.8
		21	3000±560	31.5±5.9
	Au	2.3	178±61	3.4±1.2
		4.7	740±270	14.3±5.2
		6.8	2050±130	39.5±25.9
		11	2730±560	52.7±10.7
		21	5200±1300	100±25.3
	Si	2.3	299±76	0.7±0.2
		4.7	630±70	1.5±0.2
		6.8	552±150	1.3±0.4
		11	968±280	2.3±0.7
		21	988±170	2.3±0.4
1064	Cu	2.3	18±8	0.2±0.1
		4.7	52±18	0.5±0.2
		6.8	152±37	1.4±0.3
		11	249±45	2.2±0.4
		21	442±95	3.9±0.8
	Ag	2.3	45±3	0.05±0.03
		4.7	40±21	0.4±0.22
		6.8	93±22	1.0±0.23
		11	221±44	2.3±0.46
		21	439±140	4.6±1.49
	Au*	2.3		
		4.7	-	-
		6.8		
		11	-	-
		21		
	Si	2.3	198±39	0.46±0.1
		4.7	392±90	0.91±0.2
		6.8	670±86	1.6±0.2
		11	952±120	2.2±0.3
		21	1070±200	2.5±0.5

*The gold craters at this laser wavelength were not measurable by the techniques available

Table 7.3 Optimum gate delays and gate widths for each metal at 5 different irradiances

Laser Wavelength (nm)	Sample	Irradiance (GW/cm^2)	Gate Delay (μs)	Gate Width(μs)
532	Cu	2.3	0.0	2.3
		4.7	0.0	2.3
		6.8	0.0	1.5
		11	0.0	1.0
		21	0.0	1.0
1064		2.3	0.2	2.0
		4.7	0.2	1.5
		6.8	0.2	1.5
		11	0.2	0.75
		21	0.2	0.75
532	Ag	2.3	0.15	2.0
		4.7	0.15	2.0
		6.8	0.15	1.5
		11	0.15	1.5
		21	0.0	0.5
1064		2.3	0.15	1.75
		4.7	0.15	1.75
		6.8	0.15	0.8
		11	0.15	0.8
		21	0.15	0.8
532	Au	2.3	0.0	3.0
		4.7	0.0	3.0
		6.8	0.0	1.25
		11	0.0	1.0
		21	0.0	0.75
1064		2.3	0.0	2.0
		4.7	0.0	1.25
		6.8	0.0	1.25
		11	0.0	1.25
		21	0.0	1.25
532	Si	2.3	0.0	1.5
		4.7	0.0	1.5
		6.8	0.0	0.9
		11	0.0	0.75
		21	0.0	0.75
1064		2.3	0.15	2.5
		4.7	0.15	2.5
		6.8	0.15	2.5
		11	0.0	1.0
		21	0.0	1.0

*See Table 5-2 for specific laser irradiances for each wavelength

Table 7-4 Calculated breakdown thresholds

Sample	Density ρ (g/cm^3)	Latent Heat of Vaporization L_v (J/g)	Heat Capacity C_p (J/gK)	Thermal Conductivity λ (W/m K)	Breakdown Threshold* E_{th} (MW/cm^2)
Cu	8.92	4721	0.384	3.91	407
Ag	10.49	2364	0.234	4.28	296
Au	19.3	1675	0.129	3	321
Si	2.33	12782	0.712	1.5	256

All the properties were taken from the CRC Handbook of Chemistry and Physics (65)
*Calculated from equation 2.3

Table 7-4 Change in volume ablated at 532 nm in relation to 1064nm.

Sample	Percent change in volume ablated	
	Before critical irradiance	After critical irradiance
Cu	53	174
Ag	1953	583
Au*		
Si	18	-8

*Crater volume not measurable by techniques available

Table 7-5 Experimental breakdown thresholds

Laser Wavelength (nm)	Sample	S/N Method E_{th} (GW/cm^2)	Volume Ablated Method E_{th} (GW/cm^2)	Literature Values (GW/cm^2)
532 nm	Cu	0.4	1.3	0.45^a 0.322^b
	Ag	1.5	0.1	0.316^b
	Au	0.8	2.2	0.99^a
	Si	0.08	0.12	
1064 nm	Cu	1.1	1.0	0.292^b
	Ag	2.1	2.0	0.234^b
	Au	0.9		
	Si	0.2	0.6	-
248 nm	Si			0.15^c
266 nm	Si			20^d

^{a}Taken from Petzoldt et al (51)
^{b}Taken from Cabalin et al (50)
^{c}Taken from Lu et al (66)
^{d}Taken from Lin et al (60)

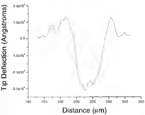

Figure 7-1 Typical profilometer scan

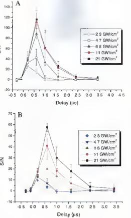

Figure 7-2 S/N ratio versus delay time for copper at two laser wavelengths (A) 532 nm, (B) 1064 nm

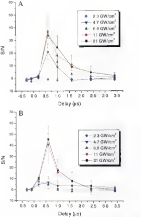

Figure 7.3 S/N ratio versus delay time for silver at two laser wavelengths (A) 532 nm, (B) 1064 nm

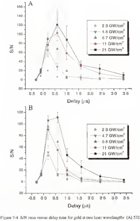

Figure 7-4 S/N ratio versus delay time for gold at two laser wavelengths (A) 532 nm (B) 1064 nm

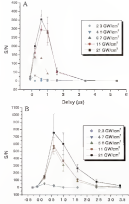

Figure 7-5 S/N ratio versus delay time for silicon at two laser wavelengths (A) 532 nm, (B) 1064 nm

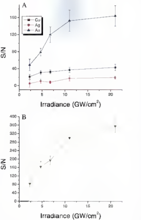

Figure 7-6 Plots of S/N versus irradiance at 532 nm. (A) Cu, Ag and Au, (B) Si

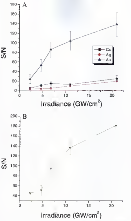

Figure 7-7 Plots of S/N versus irradiance at 1064 nm. (A) Cu, Ag and Au. (B) Si

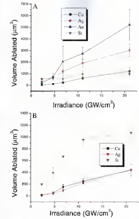

Figure 7.8 Plots of volume ablated versus irradiance (A) At 532 nm, (B) At 1064 nm.

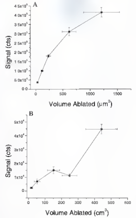

Figure 7-9 Plots of signal versus volume ablated for copper. (A) At 532 nm, (B) At 1064 nm

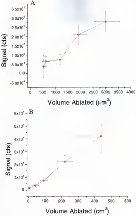

Figure 7-10 Plots of signal versus volume ablated for silver (A) At 532 nm, (B) At 1064 nm

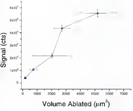

Figure 7-11 Signal versus volume ablated for gold 532 nm

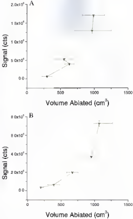

Figure 7-12 Plots of signal versus volume ablated for silicon (A) At 532 nm, (B) At 1064 nm.

CHAPTER 8
CONCLUSIONS AND FUTURE WORK

In this work, several experiments were performed in order to study laser-material interactions between a Nd:YAG laser and copper, silver, gold and silicon surfaces. Studies focused on the time development of spectral lines within a propagating plasma. Several irradiances were studied as well as two laser wavelengths, 532 nm and 1064 nm. Further studies showed the dependence of the signal-to-noise ratio on laser irradiance at both laser wavelengths. Breakdown thresholds were determined experimentally and theoretically for each sample studied. The theoretical thresholds were determined to be within one order of magnitude of the experimental values. It was also determined that the surface absorptance is an important factor that influences the ablation volume.

At the lowest laser irradiance studied (2.3 GW/cm^2), the amount of ablated material is element specific and dependent on laser wavelength. At 532 nm, the lowest ablated mass was 0.3 ng for Cu, 5.6 ng for Ag, 3.4 ng for Au and 0.7 ng for Si. At 1064 nm, the lowest ablated mass was 0.2 ng for Cu, 0.05 ng for Ag and 0.46 ng for Si. Though Au craters at 1064 nm were not measured, it can be assumed that the mass ablated was less than 3.4 ng. Table 8-1 compares the average ablated mass at 532 nm and 1064 nm with literature values. At both wavelengths, the experimental values were one order of magnitude smaller than the literature values. The average ablated mass was 2.5 ng at 532 nm and 0.2 ng at 1064 nm. In previous works, researchers have found minimum ablation masses of 50 ng at 532 nm (27) and 25 ng at 1064 nm (67). Using the microscope we were able to obtain ablation masses much smaller than earlier experiments.

Previous researches have used spatial resolution to characterize the usefulness of a technique (69). The spatial resolution is defined as the width of the ablation crater. In our experiments, the average crater width (at the lowest irradiance) was 33.4 µm at 532 nm and 17.3 µm at 1064 nm (Table 8.2). The spatial resolution found in these experiments was much smaller than values reported by previous researchers. Romero and co-workers have report values of 70 µm for a 337.1 nm N_2 laser (19) and 750 µm for a 532 nm Nd YAG laser (21). The microscope used in our experiments allowed for tighter focusing of the laser and thus increased spatial resolution. The spatial resolution obtained in LIPS is comparable to LA-ICP MS and XPS.

The use of the microscope in the experiments was essential to reducing the dimensions of analysis. The microscope increased the spatial resolution and decreased the average ablated mass for each analysis.

Further studies should focus on developing the existing LIPS instrumentation for routine spatial analysis. The instrument has been optimized for laser wavelengths of 532 nm and 1064 nm. The instrument is capable of translating a sample in step-wise fashion, sampling the surface with the laser and detecting the emitted light. Using the conditions presented in this work, a spatial resolution of 17 µm and an ablation limit of 0.2 ng are possible. A better spatial resolution might be obtained with a higher magnification objective (>10x). A commercial microscope might also offer tighter focusing. The microscope built in the lab had several design flaws.

In addition, an ideal instrument would be capable of simultaneous multielement analysis. The spectral lines used in this experiment were not contained within the same spectral window. Therefore, spectral analysis would be best achieved with an Echelle spectrometer. An Echelle spectrometer has a spectral range between 200 nm and 850 nm.

Finally, the instrument needs to be automated for routine analysis. A computer programmer could fully automate the focusing of the microscope, surface analysis and data manipulation.

In conclusion, the work presented here supports the further development of laser induced plasma spectroscopy as new analytical method for surface characterization. LIPS requires minimal or no sample preparation and can analyze any phase of matter. Unlike Auger electron spectroscopy and glow discharge techniques, LIPS analyzes conductive and insulating materials alike. LIPS is capable of localized microanalysis with micrometer resolution. LIPS also has the possibility of *in situ* measurements. It is useful in element identification and is capable of spatial resolutions on the order of 17.4 µm and ablation limits of 0.2 ng.

Table 8-1 Comparison of experimental values of ablated mass with literature values.

Laser Wavelength (nm)	Experimental Values of Ablated Mass (ng)	Literature Values of Ablated Mass (ng)
532	2.5	50[a]
1064	0.2	25[b]

[a] Taken from Milan et al (27)

[b] Taken from Kim et al (67)

Table 8-2 Comparison of experimental values of spatial resolution with literature values.

Laser Wavelength (nm)	Experimental Values of Spatial Resolution (µm)	Literature Values of Spatial Resolution (µm)
532	33.4	750[a] 70[b,*]
1064	17.3	

[a] Taken from Romero et al (21)

[b] Taken from Romero et al (19)

*With a 337.1 nm N_2 laser

LIST OF REFERENCES

(1) Shaffner, T. J., 1997 1996; American Institute of Physics

(2) O'Conner, D. J., Sexton, B. A., Smart, R. S. C. *Surface Analysis Methods In Materials Science*; Springer-Verlag: Berlin, 1992

(3) Vadillo, J. M.; Laserna, J. J. *Journal of Analytical Atomic Spectrometry* **1997,** *12* 859

(4) Vickerman, J. C. *Surface Analysis: The Principle Techniques*; John Wiley and Sons: New York, 1997

(5) Grabke, H. J., Mast, R., Ruck, A. *Process Technology Conference Proceedings* **1997,** *15*, 183

(6) Walmsey, J. C., Jones, G., Lee, B. J., Wild, R. K. *Applied Surface Science* **1997,** *108*, 289

(7) Hartmann, A. J., Lamb, R. N. *Current Opinions in Solid State Materials Science* **1997,** *2*, 511

(8) Blomberg, E., Claesson, P. M., Froberg, J. C. *Biomaterials* **1998,** *19*

(9) Froeschle, B., Glowacki, F., Bauer, A. J., Kasko, I., Oechsner, R., Schneider, C. *Proceedings of the Electrochemical Society* **1998,** *97 35*, 415

(10) Lawing, A. S., Han, Y.-P., Sawin, H. H. *Proceedings of the Electrochemical Society* **1998,** *97 35*

(11) Makohliso, S. A., Leonard, D., Giovangrandi, L., Mathieu, H. J., Ilegems, M., Aebischer, P. *Langmuir* **1999,** *15*, 2940

(12) Dunlop, H. M., Benmalek, M. *Journal de Physique IV* **1997,** *7*, 163

(13) Battaglin, C., Caccavale, F., Menelle, A., Montecchi, M., Nichelatti, E., Nicoletti, F., Polato, P. *Thin Solid Films* **1999,** *351*, 176

(14) Jeong, S. H., Borisov, O. V., Yoo, J. H., Mao, X. L., Russo, R. E. *Analytical Chemistry* **1999,** *71*, 5123

(15) Mao X ; Chan W T ; Russo R E *Applied Spectroscopy* **1997,** *51* 1047

(16) Mao, X L.; Borisov O V.; Russo R E. *Spectrochimica Acta Part B* **1998,** *53* 731

(17) Russo R E. Mao X. L. Caetano M ; Shannon M A *Applied Surface Science* **1996,** *96-98*, 144

(18) Kogan V V Hinds M W ; Ramendik, G I *Spectrochimica Acta Part B* **1996,** *49* 333

(19) Romero D , Laserna, J J *Analytical Chemistry* **1997,** *69*, 2871

(20) Romero, D , Laserna, J J *Journal of Analytical Atomic Spectrometry* **1998,** *13* 357

(21) Romero D Romero J M F , Laserna, J J *Journal of Analytical Atomic Spectrometry* **1999,** *14* 199

(22) Vadillo J M Milan M Laserna, J J *Fresenius Journal of Analytical Chemistry* **1996,** *355* 10

(23) Vadillo J M. Vadillo, I Carrasco F Laserna, J J *Fresenius Journal of Analytical Chemistry* **1998,** *361* 119

(24) Lucena, P , Vadillo J M., Laserna, J J *Analytical Chemistry* **1998,** *71*, 4385

(25) Hildago M. Martin F Laserna, J J *Analytical Chemistry* **1996,** *68* 1095

(26) Vadillo J M Garcia, C C Palanco S Laserna, J J *Journal of Analytical Atomic Spectrometry* **1998,** *13*, 793

(27) Milan, M Lucena, P Cabalin, L. M Laserna, J J *Applied Spectroscopy* **1998,** *52* 444

(28) Maiman T H *Nature* **1960,** *187* 493

(29) Ingle J D Crouch, S R. *Spectrochemical Analysis* Prentice-Hall Inc., Englewood Cliffs, 1988

(30) Miller J C , R F Haglund J *Laser Ablation and Desorption*, Academic Press San Diego 1998

(31) Ready J F *Effects of High Power Laser Radiation* Academic Press New York, 1971

(32) Brech, F., Cross, L. *Applied Spectroscopy* **1962,** *16*, 59.

(33) Allmen, M. v.; Blatter, A. *Laser Beam Interactions with Materials*; Springer Verlag: Berlin, 1995.

(34) Cremers, D. A.; Radziemski, L. J. *Laser Induced Plasmas and Applications*; Marcel Dekker, Inc.: New York, 1989.

(35) Darke, S. A.; Tyson, J. F. *Journal of Analytical Atomic Spectrometry* **1993,** *8*, 145.

(36) Ahmad, I.; Goddard, B. J. *Jurnal Fizik Malaysia* **1993,** *14*, 43.

(37) Moenke-Blankenburg, L. *Laser Microanalysis*; John Wiley & Sons: New York, 1989.

(38) Vertes, A.; Gijbels, R.; Adams, F. *Laser Ionization Mass Analysis*; John Wiley & Sons, Inc.: New York, 1993.

(39) Ready, J. F. *Applied Physics Letters* **1963,** *3*, 11.

(40) Russo, R. E. *Applied Spectroscopy* **1995,** *49*, 14A.

(41) Skoog, D. A.; Leary, J. J. *Principles of Instrumental Analysis*; Saunders College Publishing: Fort Worth, Texas, 1992.

(42) Gornushkin, I. B.; King, L. A.; Smith, B. W.; Omenetto, N.; Winefordner, J. D. *Spectrochimica Acta* **1999,** *54 B*, 1207.

(43) Krokhin, O. N. In *Laser Handbook*; Arecchi, F. T.; Schulz-Dubois, E. O., Eds. North-Holland Publishing Company: Amsterdam, 1972, Vol. 2, pp 1371-1407.

(44) Arnold, N.; Luk'yanchuk, B.; Bityurin, N. *Applied Surface Science* **1998,** *127-129*, 184.

(45) Stuart, B. C.; Feit, M. D.; Herman, S.; Rubenchik, A. M.; Shore, B. W.; Perry, M. D. *Physical Review B* **1996**, *53*, 1749.

(46) Stuart, B. C.; Feit, M. D.; Herman, S.; Rubenchik, A. M.; Shore, B. W.; Perry, M. D. *Journal of the Optical Society of America B* **1996,** *13*, 459.

(47) Linde, D. v. d.; Schuler, H. *Journal of the Optical Society of America B* **1996,** *13*, 216.

(48) Downer, M. C.; Fork, R. L.; Shank, C. V. *Journal of the Optical Society of America B* **1985,** *2*, 595.

(49) Lenzner M Kruger J Sartania, S Cheung, Z Spielman, C Mourou, G , Kautek, W Krausz, F *Physics Review Letters* **1998,** *80*, 4076

(50) Cabalin, L. M , Laserna J J *Spectrochimica Acta Part B* **1998,** *53* 723

(51) Petzoldt, S Reif, J Matthias, E. *Applied Surface Science* **1996,** *96-98* 199

(52) Marcus, S Lowder J E. Mooney, D L. *Journal of Applied Physics* **1976,** *47* 2966

(53) Niemz M H *Applied Physics Letters* **1995,** *66* 1181

(54) Apostol I Stoian R Luculescu C Dabu R Stratan, A. *Proceedings of the SPIE* **1998,** *3404*, 243

(55) Marcus S Lowder J E Manlief S Mooney D L. *IEEE Journal of Quantum Electrons* **1975,** *QE 11* 49D

(56) Hong M H Lu Y F Bong, S K *Applied Surface Science* **2000,** *154 155*, 196

(57) Lee Y L, Song K Cha, H K., Lee J M., Park, M -C , Sneddon J *Applied Spectroscopy* **1997,** *51* 959

(58) Corliss C H Bozman W R. *Experimental Transition Probabilities for Spectral Lines of Seventy Elements* U S Government Printing Office: Washington D C. 1962

(59) Man, B Y Wang X. T Liu A H *Journal of Applied Physics* **1998,** *83* 3509

(60) Liu H C Mao, X L , Yoo, J H Russo R E. *Spectrochimica Acta Part B* **1999,** *54* 1607

(61) Striganov A R Sventitskii N S *Tables of Spectral Lines of Neutral and Ionized Atoms* IFI/Plenum New York, NY 1968

(62) Shannon M A Mao X L Fernandez A Chan, W -T Russo, R E. *Analytical Chemistry* **1995** *67*, 4522

(63) Liu H C Mao X L Yoo, J H Russo, R E. *Applied Physics Letters* **1998,** *75*, 1216.

(64) Mao S S Mao X Greif R Russo R. E *Applied Physics Letters* **1998,** *73* 1331

(65) Lide, D. R. *CRC Handbook of Chemistry and Physics*. CRC Press. Boca Raton, Florida, 1995

(66) Webpage *http://www.gps.caltech.edu/genesis/Thermal_Coll.html*, 2000

(67) Kim, T., Yoon, Y., Lee, G. *Journal of the Korean Physical Society* **1999,** *35*, 198

(68) Lu, Y. F., Hong, M. H., Low, T. S. *Journal of Applied Physics* **1999,** *85*, 2899

(69) Vadillo, J. M., Planco, S., Romero, M. D., Laserna, J. J. *Fresenius Journal of Analytical Chemistry* **1996**, *355*, 909

BIOGRAPHICAL SKETCH

Gretchen E. Potts was born in Fremont, Ohio on December 17 1973 She is the middle child in a family which includes her parents, Tom and Linda, sister Karin and brother Chris. Gretchen attended high school at Avon Lake High School in Avon Lake, Ohio. She received a B S in chemistry and a minor in mathematics from Miami University at Oxford, Ohio in 1996.

I certify that I have read this study and that in my opinion it conforms to acceptable standards of scholarly presentation and is fully adequate, in scope and quality, as a dissertation for the degree of Doctor of Philosophy.

James D. Winefordner

James D. Winefordner, Chair
Graduate Research Professor of
Chemistry

I certify that I have read this study and that in my opinion it conforms to acceptable standards of scholarly presentation and is fully adequate, in scope and quality, as a dissertation for the degree of Doctor of Philosophy.

David H. Powell
Scientist

I certify that I have read this study and that in my opinion it conforms to acceptable standards of scholarly presentation and is fully adequate, in scope and quality, as a dissertation for the degree of Doctor of Philosophy.

Weihong Tan
Assistant Professor of Chemistry

I certify that I have read this study and that in my opinion it conforms to acceptable standards of scholarly presentation and is fully adequate, in scope and quality, as a dissertation for the degree of Doctor of Philosophy.

Michael J. Scott
Assistant Professor of Chemistry

I certify that I have read this study and that in my opinion it conforms to acceptable standards of scholarly presentation and is fully adequate, in scope and quality, as a dissertation for the degree of Doctor of Philosophy.

Lena Q. Ma
Associate Professor of Soil and Water
Science

This dissertation was submitted to the Graduate Faculty of the Department of Chemistry in the College of Liberal Arts and Sciences and to the Graduate School and was accepted as partial fulfillment of the requirements for the degree of Doctor of Philosophy

August 2000

Dean Graduate School

LD
1780
20 00

P871

UNIVERSITY OF FLORIDA
3 1262 08556 6098